Use of In Vivo Imaging and Physiologically-Based Kinetic Modelling to Predict Hepatic Transporter Mediated Drug–Drug Interactions in Rats

pharmaceutics

MDPI

Article

Use of In Vivo Imaging and Physiologically-Based Kinetic Modelling to Predict Hepatic Transporter Mediated Drug–Drug Interactions in Rats

Nicola Melillo [1,2,†], Daniel Scotcher [1,†], J. Gerry Kenna [3], Claudia Green [4], Catherine D. G. Hines [5], Iina Laitinen [6,7], Paul D. Hockings [7,8], Kayode Ogungbenro [1], Ebony R. Gunwhy [9], Steven Sourbron [9], John C. Waterton [3,10], Gunnar Schuetz [4] and Aleksandra Galetin [1,*]

1 Centre for Applied Pharmacokinetic Research, Division of Pharmacy and Optometry, School of Health Science, The University of Manchester, Manchester M13 9PL, UK; daniel.scotcher@manchester.ac.uk (D.S.)
2 SystemsForecastingUK Ltd., Lancaster LA1 5DD, UK
3 Bioxydyn Ltd., Manchester M15 6SZ, UK
4 MR & CT Contrast Media Research, Bayer AG, 13353 Berlin, Germany
5 GSK, Collegeville, PA 19426, USA
6 Sanofi-Aventis Deutschland GmbH, Bioimaging Germany, 65929 Frankfurt am Main, Germany
7 Antaros Medical, 431 83 Mölndal, Sweden
8 MedTech West, Chalmers University of Technology, 413 45 Gothenburg, Sweden
9 Department of Infection, Immunity and Cardiovascular Disease, University of Sheffield, Sheffield S10 2TA, UK
10 Centre for Imaging Sciences, Division of Informatics Imaging & Data Sciences, School of Health Sciences, The University of Manchester, Manchester M13 9PL, UK
* Correspondence: aleksandra.galetin@manchester.ac.uk
† These authors contributed equally to this work.

Abstract: Gadoxetate, a magnetic resonance imaging (MRI) contrast agent, is a substrate of organic-anion-transporting polypeptide 1B1 and multidrug resistance-associated protein 2. Six drugs, with varying degrees of transporter inhibition, were used to assess gadoxetate dynamic contrast enhanced MRI biomarkers for transporter inhibition in rats. Prospective prediction of changes in gadoxetate systemic and liver AUC (AUCR), resulting from transporter modulation, were performed by physiologically-based pharmacokinetic (PBPK) modelling. A tracer-kinetic model was used to estimate rate constants for hepatic uptake (k_{he}), and biliary excretion (k_{bh}). The observed median fold-decreases in gadoxetate liver AUC were 3.8- and 1.5-fold for ciclosporin and rifampicin, respectively. Ketoconazole unexpectedly decreased systemic and liver gadoxetate AUCs; the remaining drugs investigated (asunaprevir, bosentan, and pioglitazone) caused marginal changes. Ciclosporin decreased gadoxetate k_{he} and k_{bh} by 3.78 and 0.09 mL/min/mL, while decreases for rifampicin were 7.20 and 0.07 mL/min/mL, respectively. The relative decrease in k_{he} (e.g., 96% for ciclosporin) was similar to PBPK-predicted inhibition of uptake (97–98%). PBPK modelling correctly predicted changes in gadoxetate systemic AUCR, whereas underprediction of decreases in liver AUCs was evident. The current study illustrates the modelling framework and integration of liver imaging data, PBPK, and tracer-kinetic models for prospective quantification of hepatic transporter-mediated DDI in humans.

Keywords: gadoxetate; pharmacokinetics; hepatic transporters; modelling and simulation; DCE-MRI; OATP1B

Citation: Melillo, N.; Scotcher, D.; Kenna, J.G.; Green, C.; Hines, C.D.G.; Laitinen, I.; Hockings, P.D.; Ogungbenro, K.; Gunwhy, E.R.; Sourbron, S.; et al. Use of In Vivo Imaging and Physiologically-Based Kinetic Modelling to Predict Hepatic Transporter Mediated Drug–Drug Interactions in Rats. *Pharmaceutics* **2023**, *15*, 896. https://doi.org/10.3390/pharmaceutics15030896

Academic Editors: Frank Wuest and Stefan Oswald

Received: 10 January 2023
Revised: 23 February 2023
Accepted: 3 March 2023
Published: 10 March 2023

1. Introduction

Clinically relevant drug–drug interactions (DDIs) can result in potentiated or reduced efficacy, that requires drug dose adjustment. In addition, DDIs can potentially increase or reduce drug toxicity to liver or other tissues, and may arise via alterations in activities of transport proteins that mediate uptake into hepatocytes and/or biliary excretion of

drugs. For example, inhibition of the hepatic uptake transporter organic anion transporting polypeptide 1B1 (OATP1B1), by a co-administered perpetrator drug, will affect hepatic clearance of many statins and lead to elevated plasma and systemic tissue exposure, thereby causing myotoxicity [1,2]. Conversely, interaction of perpetrator drugs with hepatic transporters that mediate biliary excretion, may alter hepatocyte exposure to a victim drug without causing a measurable effect on systemic plasma exposure (e.g., metformin DDIs due to organic cation transporter 2 (OCT2) and multidrug and toxin extrusion protein (MATE)1 and MATE2-K inhibition [3]).

Quantitative translation of in vitro data through in vitro–in vivo extrapolation (IVIVE), can be undertaken via physiologically-based pharmacokinetic (PBPK) modelling, which integrates in vitro transporter kinetic/inhibition data with relevant physiological parameters [4,5]. PBPK models simulate changes in both systemic and tissue exposure of the victim drug, that arise because of changes in enzyme and/or transporter activity caused by the perpetrator drug [6,7]. These methods are used routinely to support regulatory submissions and drug labelling, and their value has been recognized in DDI and PBPK regulatory guidance documents [8–10]. However, verification of the accuracy of PBPK simulations of tissue exposure is challenging, especially for transporter DDIs where changes in drug exposure may occur within hepatocytes, but not in plasma (or not to the same extent). In particular, clinical DDI studies are usually unable to detect interactions that arise via inhibition of hepatobiliary efflux transporters, such as multidrug resistance-associated protein (MRP)2, due to the lack of a measurable effect on systemic plasma exposure [6].

Hence there is a need for additional methods to quantify effects of test drugs on transporter function in vivo. One promising approach is dynamic contrast-enhanced magnetic resonance imaging (DCE-MRI), using the contrast agent gadoxetate. Since magnetic resonance imaging (MRI) is tomographic, concentrations of gadoxetate can be simultaneously determined in plasma, liver, kidney, bile, and other compartments. Gadoxetate is administered intravenously (iv) and is eliminated exclusively via renal and biliary excretion. It is a substrate of multiple hepatocyte uptake (OATP1A1, OATP1B1, OATP1B3, and Na^+-taurocholate cotransporting polypeptide (NTCP)) and efflux (MRP2, MRP3) transporters [11–13], and has a high hepatic extraction ratio in rats. Uptake of gadoxetate in healthy hepatocytes, enhances the regional T_1-weighted magnetic resonance (MR) signal. The opposite is seen in the presence of lesions from liver metastases (non-hepatic origin). These properties have been exploited in clinical MRI, as gadoxetate is used routinely to detect and characterize lesions in adults with known or suspected focal liver disease [14].

If MR is monitored dynamically during the uptake and washout of the contrast agent, then regional gadoxetate pharmacokinetics can be derived, to probe hepatic transporter-mediated DDI in human. Data from such DCE-MRI experiments are often analyzed using multi-compartment tracer-kinetic models [6,15–20]. (An indicator is a detectable substance that is introduced into a physiological system, yielding information about the system itself. A tracer is a type of indicator chemically identical to a substance of interest but separately detectable. Gadoxetate is an indicator, but not a tracer. However, it is a common convention to refer to tracer-kinetic models as models for indicators that are not tracers, such as gadoxetate [15].) These tracer-kinetic models, unlike PBPK models, do not assess the mass balance in the whole body. Tracer-kinetic models use the systemic concentration (e.g., in arterial and/or portal venous blood vessels) as input function to a compartmental model describing only the organs or tissues of interest (e.g., the liver) [15].

PBPK models have also been applied to DCE-MRI data, although not as commonly as tracer-kinetic models [21,22]. We previously reported a PBPK model for gadoxetate in rats, developed using a combination of bottom-up (i.e., based on IVIVE) and top-down approaches. The PBPK model captured the blood, spleen, and liver gadoxetate DCE-MRI profiles of both control and inhibitory phases, following the administration of an intravenous rifampicin dose of 10 mg/kg bodyweight [23]. With the same DCE-MRI data, we also developed a compartmental tracer-kinetic model giving the kinetic rate constants for gadoxetate transport from the extracellular space into hepatocytes (k_{he}), and from hepatocytes into bile (k_{bh}). The reproducibility of the assay, and the effect of rifampicin 10 mg/kg on k_{he} and k_{bh}, were also assessed [24]. The results of this previous work showed promising use of gadoxetate as an imaging probe to investigate the effects of perpetrator drugs on hepatic transporters in rats [23,24].

The aim of the present study was to further evaluate the imaging biomarker gadoxetate, for investigation of hepatic transporter mediated DDI, using DCE-MRI data. To that end, two modelling approaches, PBPK and tracer-kinetic models, were investigated, using gadoxetate–drug interaction data obtained with six test drugs in rats. The drugs were selected for having variable in vitro potency of OATP1B inhibition and/or drug-labeling for potential to cause drug-induced liver injury (DILI), namely ciclosporin, rifampicin, bosentan, ketoconazole, asunaprevir, and pioglitazone. Appropriate doses for all the six drugs were selected by pharmacokinetic modelling and simulation. The translational modelling capabilities of the previously developed gadoxetate PBPK model [23], were assessed by comparing the prospective bottom-up prediction of the hepatic transporters DDI, with the observed gadoxetate DCE-MRI systemic and liver data in the inhibitory phases. In parallel, a tracer-kinetic model [24] was evaluated by quantifying the effect of the six drugs investigated, on gadoxetate hepatic volume transfer constant (K^{trans}), and rate constants k_{he} and k_{bh}.

2. Materials and Methods

2.1. Source of Test Chemicals

All drugs were obtained locally, from the following suppliers: Rifampicin (Eremfat® 300 mg, Riemser Pharma GmbH, Greifswald, Germany), ciclosporin (Sandimmun® 50 mg/mL, Novartis Pharma GmbH, Nuremberg, Germany), ketoconazole (HRA 200 mg, HRA Pharma Deutschland GmbH, Wiesbaden, Germany), bosentan (Sigma-Aldrich, St. Louis, MO, USA), asunaprevir (asunaprevir, MedChemExpress, Monmouth Junction, NJ, USA), and pioglitazone (pioglitazone, Merck & Co., Inc., Rahway, NJ, USA repository).

2.2. Review of Inhibitory Potency and Model-Based Dose Selection for Drugs

In vitro inhibition constants (K_i) and half maximum inhibitory concentrations (IC_{50}) of the six drugs for human transporters OATP1B1, OATP1B3, NTCP, and MRP2 and their rat homologues (rOatp1a4, rOatp1b2, rNtcp, and rMrp2), were collated from literature sources and in-house measurements.

For all the selected drugs, compartmental pharmacokinetic models were developed to inform dose selection in the DCE-MRI studies. The one-compartment, two-compartment, or three-compartment pharmacokinetic models, following intravenous and oral administration, were fitted to published pharmacokinetic data for these drugs in rats. The models assumed linear pharmacokinetics of the six drugs investigated, to allow identification of the model parameters with the limited available rat pharmacokinetic data. Subsequently, simulations with the empirical compartmental models were undertaken, to identify doses that would result in free plasma concentrations in rats, during the timescale of the MRI, that were within the range of free steady-state plasma concentrations achieved following oral therapeutic drug dosing in humans. The model equations, sources of pharmacokinetic data, parameters estimates, and criteria for the dose selection for all the drugs are reported in the Supplementary Material, Section S1.

2.3. Animal Handling and In Vivo Study Design

In vivo studies were undertaken at three sites (D, E, G1 + G2) at two different field strengths, 4.7 T (D, G2) and 7 T (E, G1). Details of the equipment used are given in [25]. Animal procedures were compliant with directive 2010/63/EU or Institutional Animal Care and Use Committee (IACUC), for studies performed in the European Union or United States, respectively. Male Wistar rats, approximately 250 g body weight at the time of ordering, were locally obtained from Charles River Laboratories, allowed to acclimate for one week prior to study initiation, socially housed in 12 h light/dark cycles, and were provided standard rat chow and water ad libitum. All studies were performed between April 2018 and November 2019. Table 1 summarizes the drugs, dose, number of animals, and the time of dosing prior to the gadoxetate injection for each site. Details of vehicle formulation and preparation of drugs for intravenous injection are listed in Supplementary Material, Section S2, Table S8. No formal sample size calculation was performed: group sizes of 4–6 were chosen, consistent with previous work, balancing reduced animal use with the ability to detect substantial treatment effects. No blinding or randomization was performed.

Table 1. Summary of gadoxetate imaging studies with six selected drugs in rats.

Drug	Dose	Number of Animals	Dose Staggering Time [a] (min)	Site (Field Strength) [b]
Rifampicin	2 mg/kg	4	60	G2 (4.7 T)
Asunaprevir	5 mg/kg	6	30	E (7 T)
Bosentan	2 mg/kg	6	60	G1 (7 T)
Bosentan	4–6 mg/kg [c]	4 [c]	60	G1 (7 T)
Ciclosporin	5 mg/kg	6	60	G2 (4.7 T)
Ketoconazole	3 mg/kg	6	30	D (4.7 T)
Pioglitazone	0.4 mg/kg	6	30	E (7 T)

[a] Time delay between dose of drug and administration of gadoxetate, informed by pharmacokinetic analysis and modelling of plasma concentration-time profiles of drugs investigated (see Supplementary Material, Section S1). [b] Sites are aligned with [25]; [c] higher dose of bosentan was explored but not tolerated well, therefore the study was discontinued, in accordance with ethics, due to adverse effects.

Drug administration and MRI acquisition were performed on animals anesthetized by inhalation of isoflurane in an air mixture, approved by each institution's animal committee, and maintained using approximately 2% isoflurane in the air mixture. Animals were monitored for respiratory rate and temperature, and a heating source, to maintain body temperature, was provided by each site. MRI was acquired in all animals on two separate days, which were separated by a washout interval of 48 h. On the first occasion, rats were dosed with vehicle (Table S8) via a tail vein catheter, using a drug-dose equivalent volume. After a drug-dependent interval (Table 1), rats were given gadoxetate (Primovist® or Eovist®, Bayer AG, Berlin, Germany), diluted 1:5 in saline and administered at 0.5 mL/kg (25 µmol/kg) over 30 s via the tail vein. On the second occasion, the procedure was repeated with a drug.

2.4. Gadoxetate DCE-MRI Data Acquisition and Elaboration

When gadoxetate is co-administered with the vehicle, the contrast agent is rapidly taken up from blood plasma into liver parenchyma, then is effluxed via bile into the gastrointestinal tract. The DCE-MRI data enable quantitative analysis of time-dependent alterations in gadoxetate concentrations in the blood and liver [26]. The imaging setup and acquisition were identical to that reported previously [24]. The DCE-MRI sequence was acquired using a T_1-weighted spoiled gradient echo sequence [17,27], with contrast agent administered after five baseline images had been acquired. Retrospective respiratory gating was employed during DCE-MRI data acquisition. On each occasion, 30 consecutive DCE-MRI measurements, including the five baseline images, were collected, at a 58 s temporal resolution, to capture the wash-in and wash-out of gadoxetate from the liver.

The derivation of DCE-MRI liver profiles employed the software PMI (Platform for research in Medical Imaging) v3.1 [28] at all the sites. DCE-MRI plasma profiles were also derived from data acquired from the spleen. Regions of interest (ROI), covering whole liver and spleen, were selected manually, as shown in Supplementary Material, Figure S10. Area under the curve ($AUC_{0\text{-}t}$) for the ΔR_1-time profiles for plasma and liver were calculated for each individual profile by using trapezoidal rule, integrating between the time of gadoxetate administration (t = 0) and the time of the last DCE-MRI measurement, where $R_1 \equiv T_1^{-1}$.

2.5. PBPK Modelling and Prospective Hepatic Transporters DDI Prediction

A previously developed reduced PBPK model of gadoxetate [23] was used in the current study. The PBPK model (Figure 1) is composed of seven compartments: blood, spleen, splanchnic organs, liver interstitial space, hepatocytes, rest of the body (ROB) vascular, and extravascular space. In the ROB compartment, muscles, fat, bones, and skin, among others, are represented.

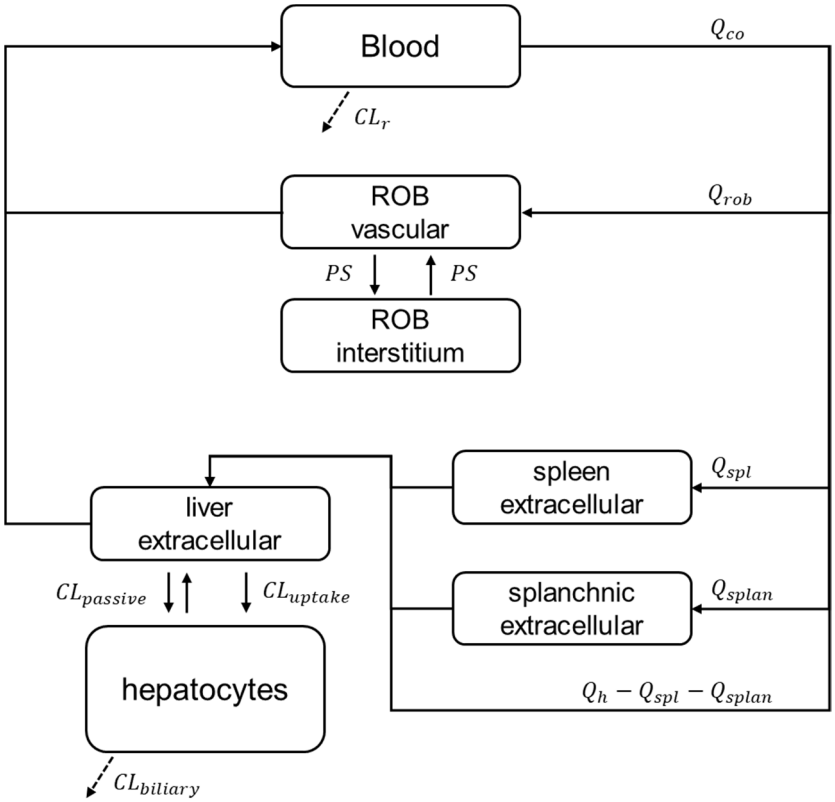

Figure 1. Structure of the reduced gadoxetate PBPK model. Continuous arrows represent the mass exchange within the system, while dashed arrows represent gadoxetate elimination. Subscripts co, rob, spl, splan, h, and r, represent cardiac output, rest of the body, spleen, splanchnic organs, hepatic and renal, respectively. CL, Q, and PS, represent the clearance processes, the blood flows, and the permeability surface product, respectively. Reproduced from [23] under CC-BY license.

A permeability-limited liver model [29] was applied to describe the gadoxetate active uptake into the hepatocytes, as per Equation (1).

$$\begin{aligned} V_{liv,extr}\frac{dc_{liv,extr}}{dt} &= input_{splan} + input_{art} - Q_h\frac{c_{liv,extr}}{K_{liv,\ extr-b}} - CL_{uptake}\cdot c_{liv,extr} - CL_{passive}(c_{liv,extr} - \\ &\qquad f_{u,liv,\ cell}\ c_{liv,cell}) \\ V_{liv,cell}\frac{dc_{liv,cell}}{dt} &= CL_{uptake}\ c_{liv,extr} + CL_{passive}(c_{liv,extr} - f_{u,liv,\ cell}\ c_{liv,cell}) - CL_{biliary}\ f_{u,liv,cell}\ c_{liv,cell} \end{aligned} \quad (1)$$

$c_{liv,extr}$, $c_{liv,cell}$ [µmol/L] and $V_{liv,extr}$, $V_{liv,int}$ [L] are the gadoxetate concentrations (c) and volumes (V) of the liver extracellular space and hepatocytes, respectively. Considering the liver fenestrated capillaries, and that gadoxetate does not distribute into red blood cells,

$V_{liv,extr}$ was defined as the sum of liver plasma and interstitial volumes. Q_h [L/h] is the sum of the portal vein and hepatic artery blood flow; CL_{uptake}, $CL_{passive}$, and $CL_{biliary}$ [L/h] are the active and passive uptake clearances across the hepatocyte sinusoidal cell membrane, and the excretion clearance from the hepatocytes to the bile, respectively; $f_{u,liv,cell}$ is the unbound fraction of gadoxetate in the hepatocytes; $K_{liv,\ extr-b}$ is the extracellular liver to blood partition coefficient; $input_{splan}$ and $input_{art}$ [µmol/h] are the portal vein and hepatic artery inputs to the liver, respectively. The model assumes no enterohepatic recirculation of gadoxetate following hepatobiliary excretion. Details of the model development, relations between concentrations in PBPK compartments and measured ΔR_1, parameters identification, and performance were described previously [23].

The inhibition of CL_{uptake} and $CL_{biliary}$ were prospectively predicted according to Equation (2) [30].

$$CL_{transporter,inh} = \frac{CL_{transporter}}{1 + c_{u,p}(t)/IC_{50}} \quad (2)$$

$CL_{transporter}$ and $CL_{transporter,inh}$ are the non-inhibited (baseline) and inhibited transporter intrinsic clearance (either CL_{uptake} or $CL_{biliary}$); $c_{u,p}(t)$ is the plasma unbound concentration of the perpetrator at a given time t, simulated with the pharmacokinetic models (Supplementary Material, Section S1); IC_{50} is the in vitro measure of the potency of the perpetrator in inhibiting the respective hepatic transporter (rOatp1b2 for active uptake, and rMrp2 for biliary efflux). IC_{50} and K_i data were collated from the literature and in-house measurements. When multiple sources were available, the prospective predictions used the lowest values of either IC_{50} or K_i to account for the worst-case scenario. Due to paucity of inhibition data for some of the drugs investigated for rat transporters, data obtained for the respective human transporters (OATP1B1 and MRP2) were used as a surrogate where necessary. The renal excretion clearance of gadoxetate (CL_r) was assumed to be unaffected by the test drugs. The performance of the prospective prediction using the PBPK modelling was evaluated by comparing the simulated gadoxetate AUC ratios ($AUCR$) in the plasma (derived from spleen compartment) and liver with the observed values. The $AUCR$ is defined as shown in Equation (3).

$$AUCR_\tau = \frac{AUC_{\tau,\Delta R_1,treated}}{AUC_{\tau,\Delta R_1,control}} \quad (3)$$

$AUC_{\tau,\Delta R_1,control}$ is the AUC of the gadoxetate ΔR_1 in tissue τ when administered alone, while $AUC_{\tau,\Delta R_1,treated}$ is the equivalent when gadoxetate is administered following a given perpetrator. The AUCs were calculated from the administration of gadoxetate ($t = 0$ min) until the end of the experiment ($t = 25$ min).

When applied to $CL_{biliary}$, Equation (2) assumes that the unbound concentration of drug at the site of inhibition of hepatobiliary efflux transporter on the canalicular, is equal to the unbound concentration of the drug in plasma ($c_{u,p}$). Previous reports have shown that some of the drugs investigated here accumulate in hepatocytes (e.g., rifampicin, ciclosporin). Therefore, for selected drugs, an alternative inhibition model was explored, taking also into account their unbound concentration ratio between hepatocyte and plasma (Kpuu) (Supplementary Material, Section S4).

2.6. Tracer-Kinetic Model and K^{trans}, k_{he}, and k_{bh} Calculation

The tracer-kinetic model was developed to enable estimation of rate constants of hepatobiliary efflux from DCE-MRI profiles in individual animals. In this approach, the liver was assumed to consist of two compartments, the extracellular space (e) and the hepatocytes (h). Since water exchanges rapidly between those spaces, the change in relaxation rate was a weighted average (Equation (4)) [31,32].

$$\Delta R_1(t) = r_{1,e} \cdot v_e \cdot c_e(t) + r_{1,h} \cdot v_h \cdot c_h(t) \quad (4)$$

The proportionality constant, $r_{1,\tau}$ $\left[\mathrm{L} \cdot \mathrm{mmol}^{-1} \cdot \mathrm{s}^{-1}\right]$, is the relaxivity of the contrast agent for the compartment τ (extracellular space, e or hepatocytes, h) at the respective field strength, while v_τ [mL/mL tissue] is the volume fraction of the compartment τ. Previously measured ex vivo $r_{1,tau}$ values for gadoxetate were used in this work [32], as per [23]. The underlying assumptions of the PBPK and tracer-kinetic models, relating to physiological volumes and perfusion, are consistent, despite different parameterizations according to the purpose of each model. For example, $V_{liv,extr}$ in the PBPK model is defined as an absolute volume (units = L; sum of liver plasma and interstitial volumes), while in the tracer-kinetic model, v_e is a volume fraction (dimensionless), defined as $V_{liv,extr}/V_{liver}$, where V_{liver} is the total liver volume. While some analogy can be drawn between CL_{active} and k_{he}, and $CL_{biliary}$ and k_{bh}, the interpretations are distinct. For example, the operating concentrations of the PBPK parameters CL_{active} and k_{he}, and $CL_{biliary}$ are the unbound concentrations of gadoxetate in plasma and hepatocytes, while the tracer-kinetic model is parameterized with respect to the total concentration of gadoxetate.

Since $c_e(t)$ is the input to the hepatocytes, and no backflux from hepatocytes to extracellular space is assumed, Equation (5) can be derived.

$$v_h \cdot c_h(t) = e^{-\frac{t}{T_h}} * k_{he} \cdot c_e(t) \quad (5)$$

where T_h is the mean transit time of gadoxetate in the hepatocytes [min], and * is convolution. The extracellular space is assumed to be in equilibrium with the blood pool and therefore the concentration $c_e(t)$ is proportional to the concentration $c_p(t)$ in the plasma of the feeding artery, i.e., $c_e(t) = (1 - E) \cdot c_p(t)$, where E is the extraction fraction of gadoxetate in the liver. Combining this assumption with Equations (4) and (5), and using $(1 - E) \cdot k_{he} = E \cdot F_p$, with F_p being the apparent plasma flow into the liver $[mL/min/mL\ tissue\ volume]$, gives Equation (6), the operational equation for gadoxetate DCE-MRI in the liver.

$$\Delta R_1(t) = (1 - E) \cdot v_e \cdot r_{1,p} \cdot c_p(t) + E \cdot F_p \cdot r_{1,h} \cdot e^{-t/T_h} * c_p(t) \quad (6)$$

Sensitivity analyses demonstrated that, with data sampled at 1 min time intervals, the amplitudes of both terms could not be measured separately, and therefore the fitted parameters were E and T_h, whereas v_e and F_p were fixed to literature values. The rate constants were derived as $K^{trans} = E \cdot F_p$, $k_{he} = E \cdot F_p/(1 - E)$, and $k_{bh} = v_h/T_h$, with a literature value for v_h. The plasma concentrations $c_p(t)$ were not reliably measured in small animals due to the small diameter of the main vessels compared to the resolution of the measurement. Therefore, spleen data were used in some instances, as a substitute (as per PBPK analysis), but these were found to be unreliable when applied for tracer-kinetic modelling in this study (not shown). Therefore, the source term $c_p(t)$ was derived from a two-compartment pharmacokinetic model for gadoxetate (see Supplementary Material, Section S5), and a step function as input in the blood compartment. The parameters k_{bh} and k_{he} were fitted to the liver data using a model implementation in Python [33]. For each rat considered in these studies, the rate constants K^{trans}, k_{he}, and k_{bh} were calculated, in both control and inhibitory phases. The rate constants of the control and inhibitory phases were compared via calculation of simple (unstandardized) effect sizes (i.e., simple effect size = $\mu_{control} - \mu_{treatment}$, where μ is the mean average of all subjects) at the 95% confidence

level. Statistical significance was assessed through a two-sided paired t-test, with $p < 0.05$ considered significant.

3. Results

In the current study, an integrated framework of in silico study design and model-based analysis was applied for gadoxetate DCE-MRI evaluation of hepatobiliary DDI in rats (Figure 2).

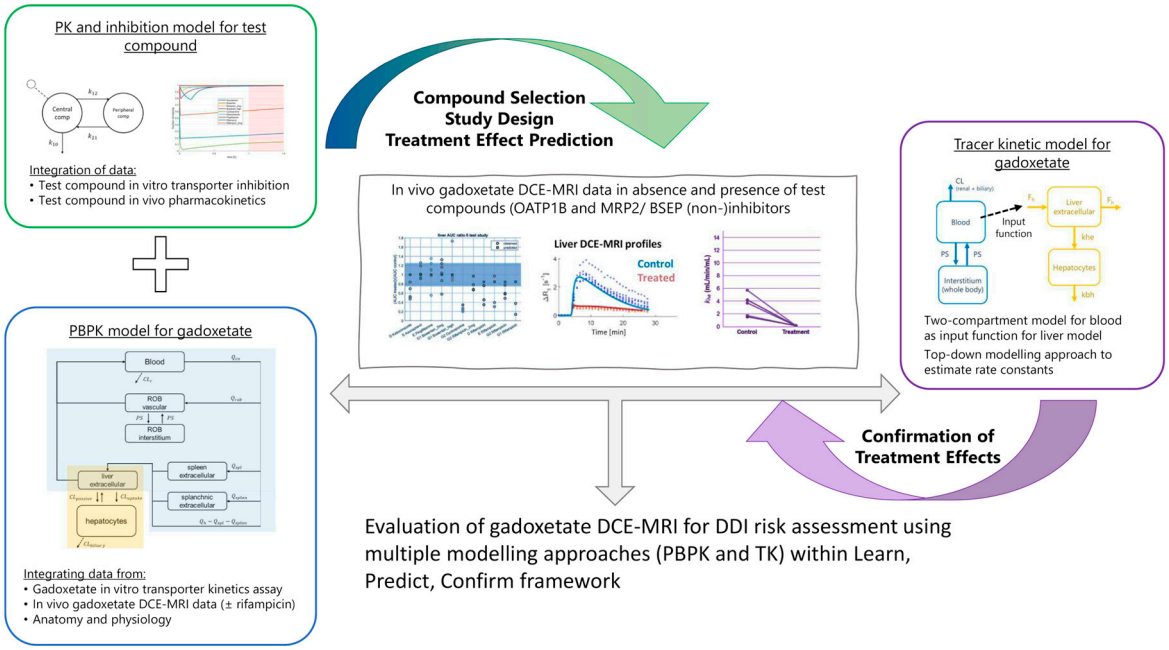

Figure 2. Framework for gadoxetate dynamic contrast enhanced magnetic resonance imaging (DCE-MRI)-based evaluation of hepatobiliary drug–drug interactions (DDI). The framework embeds modelling and simulation techniques, including physiologically-based pharmacokinetic (PBPK) and tracer-kinetic (TK) modelling throughout the study, from study design through to data analysis.

3.1. Drug Inhibitory Potency and Model-Based Dose Selection

In vitro inhibition data (e.g., IC_{50} and K_i) from the literature, for rat hepatobiliary transporters rOatp1a4, rOatp1b2, rNtcp, and rMrp2 are summarized in Table 2, while the corresponding data for human OATP1B1, OATP1B3, NTCP, and MRP2 transporters are summarized in Table 3. In vitro inhibition data in rats were available for rifampicin and ciclosporin, but were scarce for the other drugs, whereas data were available in most cases for the human transporters. For the limited number of transporters where in vitro inhibition potencies were reported in both rat and human, data were generally consistent, with the exception of the ciclosporin IC_{50} for rOa1p1a4 and rOatp1b2, which were higher than reported values for this drug with the human OATP1B transporters.

The published OATP1B1 and/or OATP1B3 IC_{50} values of bosentan, pioglitazone, asunaprevir, and ketoconazole were lower than the unbound plasma concentrations achieved at steady state following oral therapeutic administration of the drugs in humans. As there were no data for rOatp1 transporters for these drugs, no OATP1B DDI was anticipated. Conversely, based on in vitro data, rifampicin and ciclosporin were expected to inhibit rOatp1/OATP1B, supported also by clinical evidence of OATP1B mediated DDIs [30,34]. Two drugs (ciclosporin and pioglitazone) also exhibited similar potencies of NTCP inhibition (Table 3).

Table 2. In vitro inhibition constants (K_i [μM]) and half maximal inhibitory concentrations (IC_{50} [μM]) for selected drugs, against a range of rat hepatic uptake and biliary efflux transporters. Data were extracted from published literature [35–42].

Drug	K_i (μM) rOatp1a4	IC_{50} (μM) rOatp1a4	IC_{50} (μM) rOatp1b2	IC_{50} (μM) rOatp1b2	IC_{50} (μM) rNtcp	IC50 (μM) rMrp2
Rifampicin	2.9	1.3	0.79	0.6–1.1	NA	20–53
Asunaprevir	NA	NA	NA	NA	0.6	11
Bosentan	NA	NA	NA	NA	0.4	NI
Ciclosporin	NA	3–30	1.2	NA	1.5	5–15
Ketoconazole	NA	NA	NA	NA	NA	NA
Pioglitazone	NA	NA	NA	NA	NA	NA

NA—no data available; NI—reported not to inhibit the transporter.

Table 3. In vitro inhibition constants (K_i) and half maximal inhibitory concentrations (IC_{50}) for selected drugs, against a range of human hepatic uptake and biliary efflux transporters and respective maximum unbound drug plasma concentrations ($C_{max,u}$) in humans. Data were extracted from published literature [30,43–49], regulatory review and prescribing documents [50–55], and in-house data from Merck & Co., Inc., Rahway, NJ, USA.

Drug	K_i (μM) OATP1B1 [a]	IC_{50} (μM) OATP1B1 [a]	IC_{50} (μM) OATP1B3	IC_{50} (μM) NTCP	K_i (μM) MRP2 [a]	IC_{50} (μM) MRP2 [a]	C_{max} (μM) [Daily Dose]	fu
Rifampicin	0.67 (0.22–17)	1.90 (0.24–120)	0.11	277	24.3 (7.9–40.6)	55 (14.7–144)	0.85 [600 mg]	0.2
Asunaprevir	NA	0.55 (0.3–0.79)	0.65	NA	NA	4	0.76 [200 mg]	0.012
Bosentan	NA	6.6 (5.0–8.2)	5.2	18	NA	>100	3.3 [250 mg]	<0.02
Ciclosporin	0.014 (0.22–2.32)	0.50 (0.02–3.5)	0.032	0.37	4.7 (21–24)	2.7 (5.6–45.3)	1.5 [4 mg/kg]	0.1
Ketoconazole	50.7 (11.5–107.7)	15.4 (1.8–60.9)	3.9	202	NA	>20	6.6 [200 mg]	0.01
Pioglitazone	NA	5.09 (11.1–39.6)	3.41	4.04	NA	>133	4.8 [30 mg]	<0.01

[a] Key transporters for gadoxetate hepatobiliary disposition.

3.2. DCE-MRI Interaction Data

The majority of rats used in the procedures survived until the end of the study without adverse effects. Higher doses of bosentan (4–6 mg/kg) were explored, but were not tolerated well and therefore the study was discontinued, in accordance with ethics, due to adverse effects. In this study, n = 3 animals received 4 mg/kg bosentan, and n = 1 received 6 mg/kg, and contributed data to the final analysis. An ROI could not be obtained for the spleen in the animal that received 6 mg/kg. Data from two additional animals were not analyzable (n = 1 from asunaprevir study; n = 1 from ketoconazole study) and therefore did not contribute to the final analyses.

Ciclosporin and, to a lower extent, rifampicin (2 mg/kg) and ketoconazole were associated with a decrease in maximum ΔR_1 and AUC of gadoxetate ΔR_1 in the liver compared with the vehicle control, while no relevant changes were noted for any of the other drugs (Figure 3). The plasma and liver gadoxetate *AUCR* for all the drugs investigated in this study are reported in Table 4, including also data following a rifampicin dose of 10 mg/kg, as reported previously [24]. Reduced active uptake of gadoxetate into the liver in the presence of some of the inhibitors resulted in a corresponding increase in gadoxetate exposure in the plasma (Figure 4). For example, ciclosporin caused a 1.94-fold increase in gadoxetate plasma, *AUC* (1.57–3.38) and median fold decrease in gadoxetate liver *AUC* of 3.85 (3.7–5). Similar results were obtained for rifampicin dosed at 10 mg/kg. In contrast, rifampicin dosed at 2 mg/kg showed a weaker effect on both liver and plasma AUCs. All the other drugs showed a marginal effect on gadoxetate plasma and liver AUCs, with the exception of ketoconazole and a high dose of bosentan (4–6 mg/kg). Interestingly, the study arm treated with ketoconazole showed a median *AUCR* for plasma and liver equal to 0.68 (0.38–0.87) and 0.52 (0.47–0.84), respectively. Across all drugs and studies, the *AUCR* had a moderate to high inter-individual variability, with a median (range) coefficient of variation (%CV) of 33% (14–103%) and 26% (8–64%) for plasma and liver, respectively

(Table 4). These results, with the exception of ketoconazole, are in agreement with the inhibitory potency reported in the literature for these drugs, and the simulations of the inhibited fraction by individual transporters performed with the empirical compartmental model for the drugs (see Supplementary Material, Section S1).

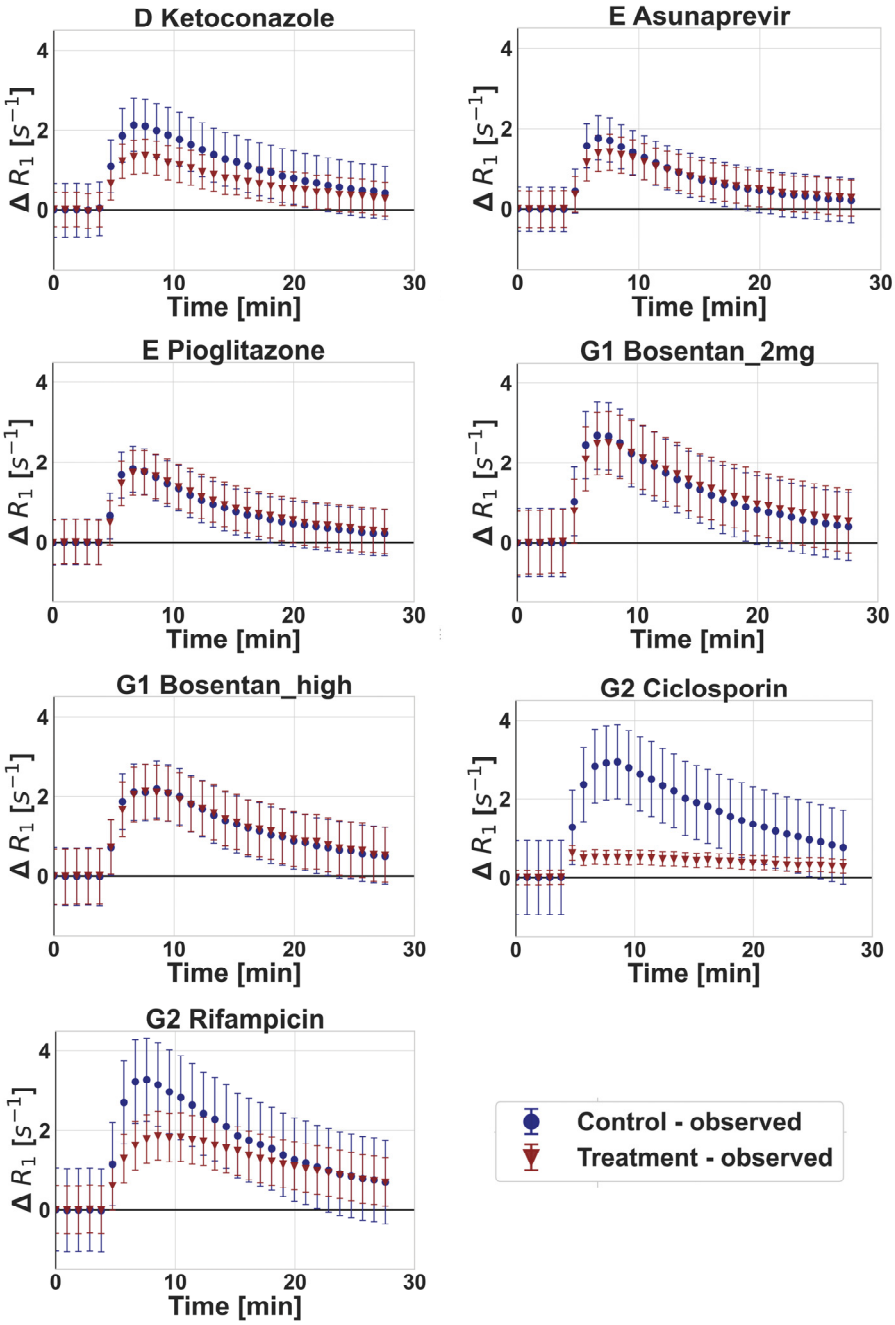

Figure 3. Observed gadoxetate liver profiles in control phase and following administration of drugs (treatment) at different sites (D, E, G1, and G2). Symbols and error bars represent mean and standard deviation (between 3 and 6 animals), respectively. Doses for each drug are listed in Table 1, where Bosentan_2mg and Bosentan_high refer to the 2 mg/kg and 4–6 mg/kg doses of bosentan, respectively.

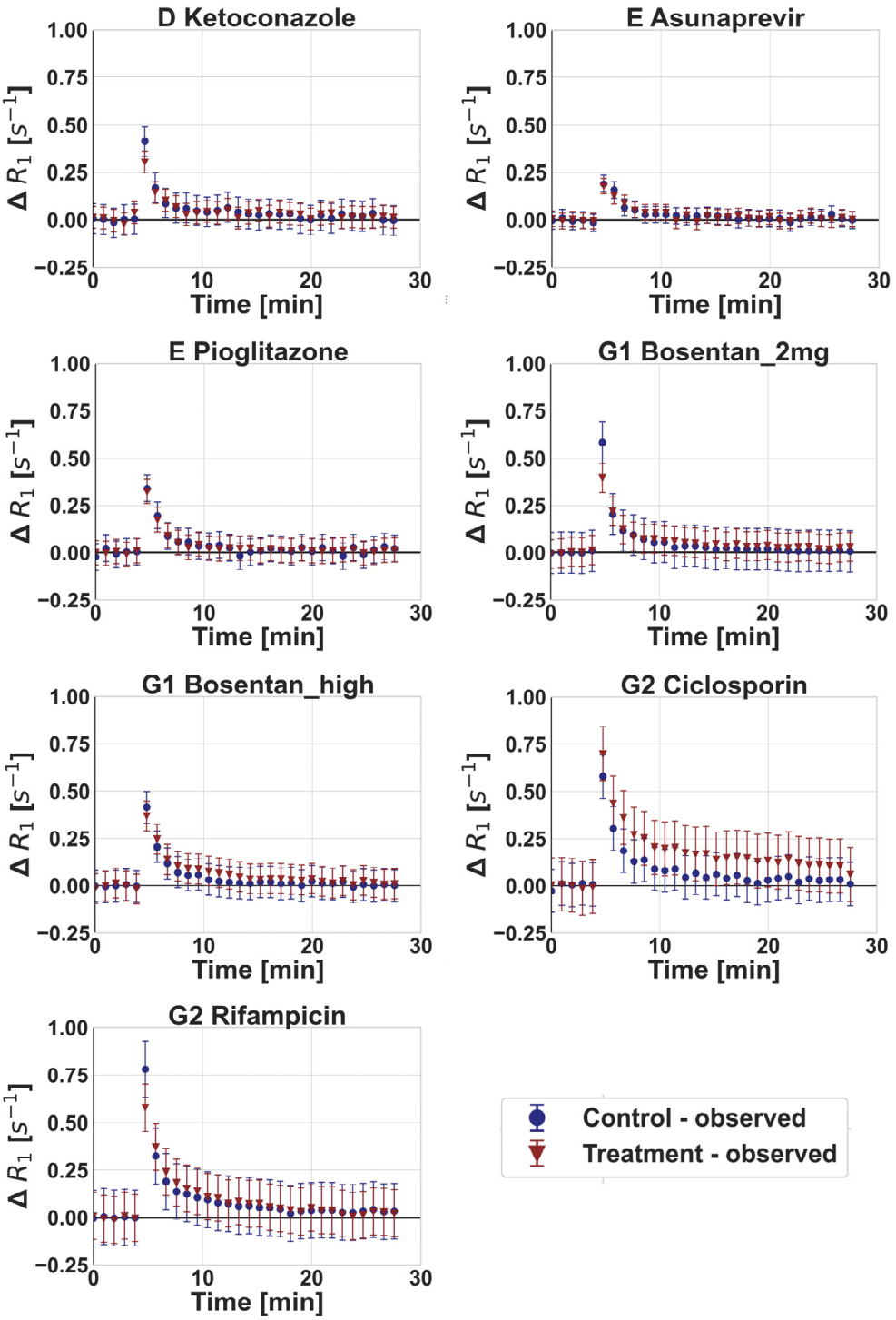

Figure 4. Observed gadoxetate plasma profiles in control phase and following administration of drugs (treatment) at different sites (D, E, G1, and G2). Symbols and error bars represent mean and standard deviation (between 3 and 6 animals), respectively. Doses for each drug are listed in Table 1, where Bosentan_high refers to the 4–6 mg/kg doses of bosentan.

Table 4. Observed and physiologically-based pharmacokinetic model (PBPK) based prediction of the ratio of gadoxetate area under the curve, based on ΔR_1, in the presence of investigated drugs relative to the vehicle control (AUCR), in plasma and liver.

Site and Drug [a]	Plasma [b]		Liver	
	Observed *AUCR* Median (min, max) [%CV; n [c]]	Predicted *AUCR*	Observed *AUCR* Median (min, max) [%CV; n [c]]	Predicted *AUCR*
D Ketoconazole 3 mg/kg	0.68 (0.38, 0.87) [30%; n = 5]	1.00	0.52 (0.47, 0.84) [26%; n = 5]	1.00
E Asunaprevir 5 mg/kg	1.12 (0.48, 4.66) [103%; n = 6]	1.01	1.01 (0.91, 1.26) [15%; n = 6]	1.00
E Pioglitazone 0.4 mg/kg	0.94 (0.6, 1.27) [25%; n = 6]	1.00	1.1 (0.55, 1.35) [26%; n = 6]	1.00
G1 Bosentan 2 mg/kg	1.09 (0.95, 1.33) [14%; n = 6]	1.00	1.1 (0.58, 1.32) [27%; n = 6]	1.00
G2 Bosentan 4–6 mg/kg	2.25 (0.92, 2.5) [45%; n = 4]	1.00	0.95 (0.88, 1.73) [40%; n = 4]	1.00
G2 Ciclosporin 5 mg/kg	1.94 (1.57, 3.38) [33%; n = 6]	3.39	0.26 (0.2, 0.27) [12%; n = 6]	0.38
G2 Rifampicin 2 mg/kg	0.92 (0.84, 1.6) [33%; n = 4]	1.15	0.68 (0.67, 0.78) [8%; n = 4]	0.98
D Rifampicin 10 mg/kg [24]	1.82 (1.44, 3.48) [48%; n = 3]	1.62	0.45 (0.35, 0.76) [41%; n = 3]	0.90
E Rifampicin 10 mg/kg [24]	2.06 (1.28, 2.35) [29%; n = 3]	1.62	0.4 (0.31, 0.97) [64%; n = 3]	0.90
G2 Rifampicin 10 mg/kg [24]	2.24 (1.24, 5.73) [70%; n = 4]	1.62	0.59 (0.49, 0.77) [20%; n = 4]	0.90
G1 Rifampicin 10 mg/kg [24]	1.45 (1.45, 4.93) [77%; n = 3]	1.62	0.38 (0.14, 0.45) [50%; n = 3]	0.90

[a] Letters indicate the site of the study, as detailed in [25]; [b] derived from DCE-MRI data acquired in spleen, see methods. [c] Coefficient of variation (%CV) [standard deviation/mean] and number (n) of animals.

3.3. Prospective Prediction of Gadoxetate Hepatic Transporter-Mediated DDIs with PBPK Model

Gadoxetate liver and plasma *AUCR* were prospectively predicted using the PBPK model for this imaging biomarker, coupled with the pharmacokinetic models for all the considered perpetrators. Comparison of predicted versus observed gadoxetate *AUCR* for the plasma and liver are reported in Table 4 and in Figure 5, respectively. Predicted versus observed ΔR_1 profiles in plasma and liver are shown in Figure 6.

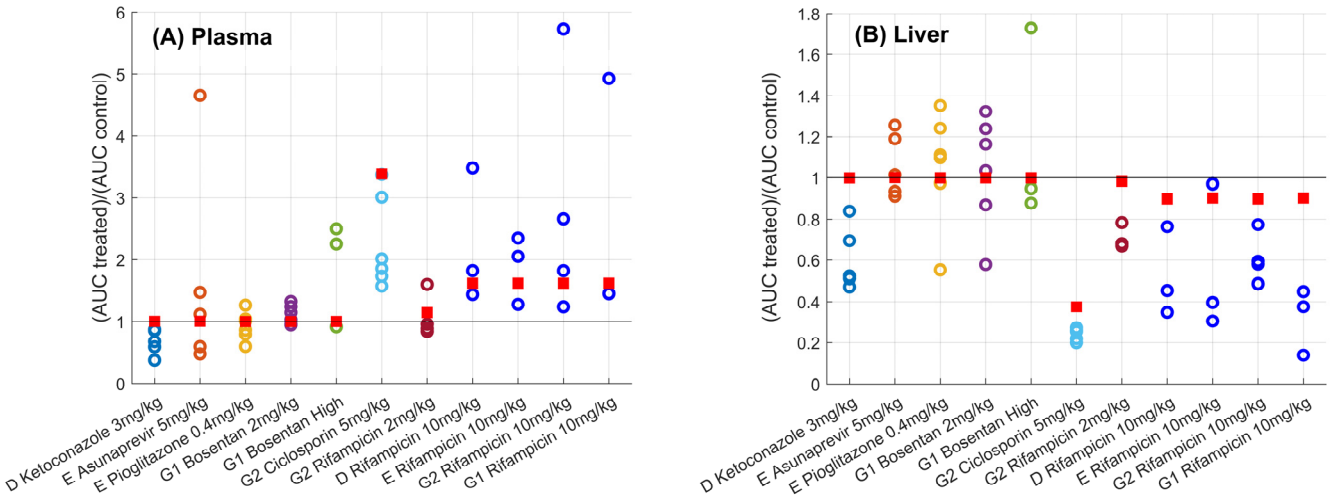

Figure 5. Predicted (■) versus observed (○) plasma (Panel **A**) and liver (Panel **B**) *AUCR* for different sites (D, E, G1, and G2) and drugs. Solid black line corresponds to the line of unity. Predictions using the gadoxetate physiologically-based pharmacokinetic model considered inhibition of both CL_{active} and $CL_{biliary}$, assuming unbound plasma concentrations to drive inhibition of each transporter of interest. *AUCR* = ratio of treated vs. control area under the curve of gadoxetate ΔR_1-time profiles (Equation (3)). Doses for each drug are listed in Table 1; "Bosentan_high" refers to the 4–6 mg/kg doses of bosentan.

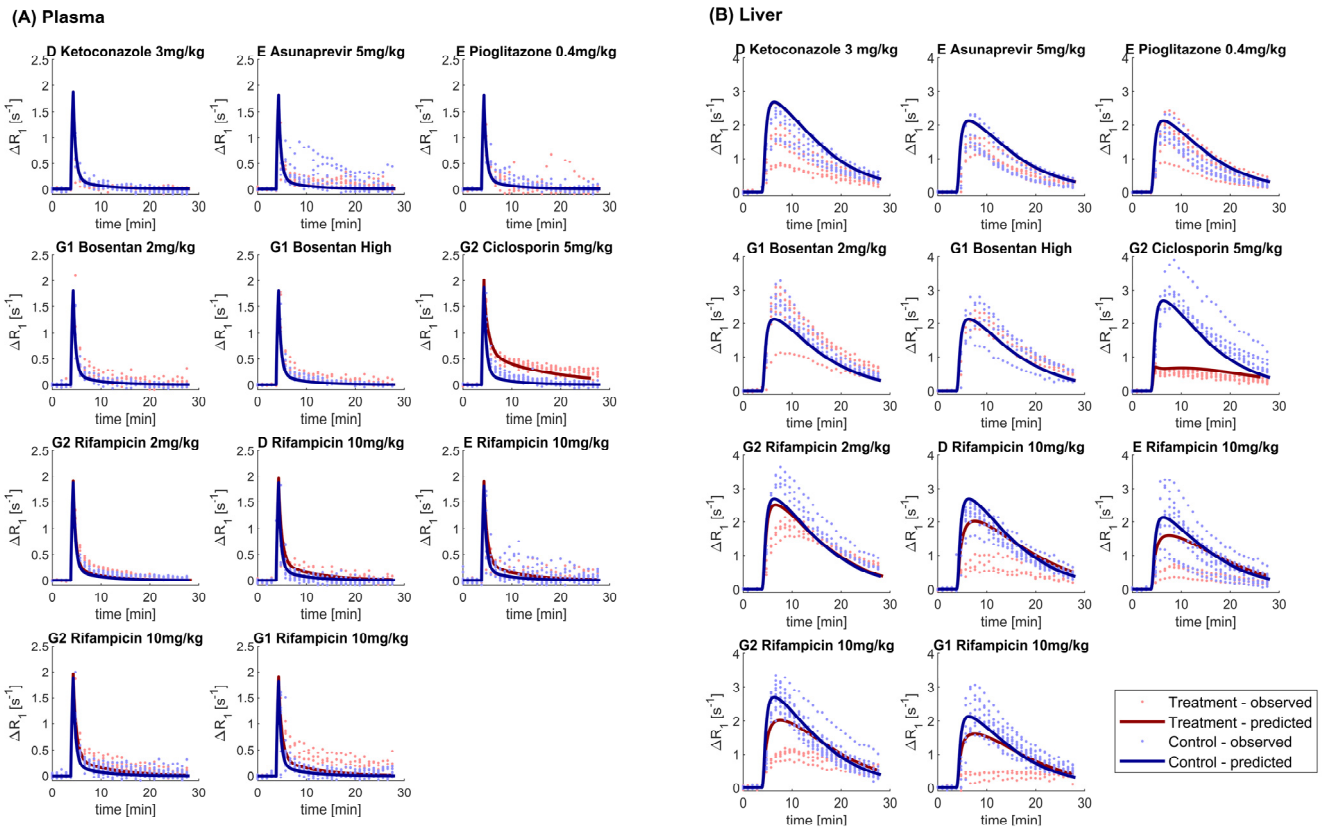

Figure 6. Predicted versus observed ΔR_1-time profiles for different sites (D, E, G1, and G2) and perpetrators (asunaprevir, bosentan, ciclosporin, ketoconazole, pioglitazone, and rifampicin) in plasma (Panel **A**) and liver (Panel **B**). Predictions using the gadoxetate physiologically-based pharmacokinetic model considered inhibition of both CL_{uptake} and $CL_{biliary}$, assuming unbound plasma concentrations to drive inhibition of each transporter parameter. Doses for each drug are listed in Table 1; "Bosentan High" refers to the 4–6 mg/kg doses of bosentan.

The PBPK model predicted well the gadoxetate ΔR_1 plasma profiles in the control phase (Figure 6A). The between-site variability was limited and therefore the mean profile simulated with the PBPK model was sufficient to capture the systemic gadoxetate pharmacokinetics. When gadoxetate was co-administered with ciclosporin and rifampicin, the inhibition of gadoxetate liver uptake clearance was accompanied by an increase in ΔR_1 in the terminal phase of the plasma profile, which was predicted successfully by the PBPK model (Figure 6A). The PBPK model coupled with the perpetrators compartmental models, predicted reasonably well the change in gadoxetate plasma AUC for ciclosporin, and lack of change in AUC for asunaprevir, pioglitazone, and bosentan. This approach also captured the effect of rifampicin as a function of the dose: for a 2 mg/kg dose the model correctly predicted a lack of interaction ($AUCR < 1.25$) and increase in the DDI at 10 mg/kg, although the magnitude was under-predicted (predicted $AUCR = 1.62$ vs. 1.89; average of four studies, Table 4).

Gadoxetate liver profiles in the control phase showed a high between-site variability, in agreement with previous reports [24]. As a result, PBPK modelling either slightly underpredicted or overpredicted the control liver profiles (Figure 6B), depending on the observed data used for comparison. PBPK modelling was able to distinguish negative controls from the OATP1B inhibitors, e.g., it predicted correctly a strong inhibition and change in gadoxetate liver AUC in the presence of ciclosporin and no inhibition in the case of asunaprevir, pioglitazone, and bosentan. Conversely, for ketoconazole, the PBPK model predicted no effect on gadoxetate liver AUC, in contrast to the observed decrease in the liver *AUC* (Figure 5). For rifampicin, the PBPK model tended to underestimate the

extent of the effect on gadoxetate liver *AUC*, as the predicted liver *AUCR* was between 1.4- and 2.4-fold higher than the median of those observed. A similar tendency, but to a lower extent, was noted for ciclosporin, where a 1.5-fold difference was seen between the predicted and observed *AUCR*.

3.4. Tracer-Kinetic Model Based Analysis

The effects of the six drugs on K^{trans}, k_{he}, and k_{bh} of gadoxetate in rats in vivo, as estimated via the tracer-kinetic modelling, are shown in Figure 7. Simple effect sizes calculated from these values are shown in Table 5.

Following administration of ciclosporin, a marked and statistically significant decrease was observed on average in gadoxetate K^{trans} (−89%, $p < 0.001$), k_{he} (−96%, $p = 0.006$), and k_{bh} (−59%, $p = 0.002$). To a lesser extent, statistically significant decreases in gadoxetate parameters were observed following administration of rifampicin, with changes in K^{trans} (−57%, $p < 0.001$), k_{he} (−90%, $p = 0.01$), and k_{bh} (−43%, $p = 0.008$). In the case of ketoconazole, decreases in K^{trans} (−46%, $p = 0.009$) and k_{he} (−65%, $p = 0.006$) were apparent, whereas no significant changes were detected in k_{bh} ($p = 0.39$). Statistically significant reductions were also observed in k_{bh} following dosing to rats of pioglitazone ($p = 0.01$) and asunaprevir ($p = 0.04$), however this was not observed in K^{trans} or k_{he} for these drugs.

No statistically significant effects on either K^{trans} or k_{bh} were detected following administration of either of the bosentan doses. This trend was also evident for k_{he} following administration of the bosentan high dose. A firm conclusion could not be obtained regarding changes in k_{he} following administration of the bosentan 2 mg/kg dose, as physiologically plausible values over both control and treatment days were only obtained for one animal ($k_{he} > 37$ mL/min/mL for all other animals).

Table 5. Absolute effects of drugs on hepatic plasma clearance (K^{trans}), hepatic uptake (k_{he}), and biliary efflux (k_{bh}) of gadoxetate as estimated using the tracer-kinetic model. Any statistically meaningful changes (where zero falls outside of the 95% CI) are marked using bold font.

Site and Drug [b]	Simple Effect Size (95% CI) [mL/min/mL Liver] [a]		
	K^{trans}	k_{he}	k_{bh}
D Ketoconazole 3 mg/kg [c]	**0.35 ** (0.20, 0.49)**	**1.27 ** (0.81, 1.74)**	0.02 (−0.02, 0.06)
E Asunaprevir 5 mg/kg [c]	0.24 (−0.01, 0.48)	2.34 (−0.92, 5.60)	**0.09 * (0.03, 0.14)**
E Pioglitazone 0.4 mg/kg	0.13 (−0.05, 0.32)	1.21 (−0.10, 2.51)	**0.05 ** (0.03, 0.08)**
G1 Bosentan 2 mg/kg [d]	0.28 (−0.32, 0.88)	−54.22 (−197.97, 89.53)	**0.07 (0.03, 0.12)**
G2 Bosentan 4–6 mg/kg	0.07 (−0.12, 0.26)	1.07 (−1.13, 3.26)	0.02 (−0.02, 0.07)
G2 Ciclosporin 5 mg/kg	**0.83 ** (0.70, 0.97)**	**3.78 ** (2.16, 5.4)**	**0.09 ** (0.06, 0.11)**
G2 Rifampicin 2 mg/kg	**0.64 ** (0.56, 0.71)**	**7.20 * (4.49, 9.91)**	**0.07 ** (0.05, 0.10)**

** $p < 0.01$; * $p < 0.05$; [a] positive value indicates a decrease in the parameter compared with control; [b] letters indicate the site of the study, as detailed in [25]; [c] subject 1 excluded from calculations due to issues with data quality during treatment; [d] subjects 3, 4, and 6 excluded from calculations due to computational fitting errors.

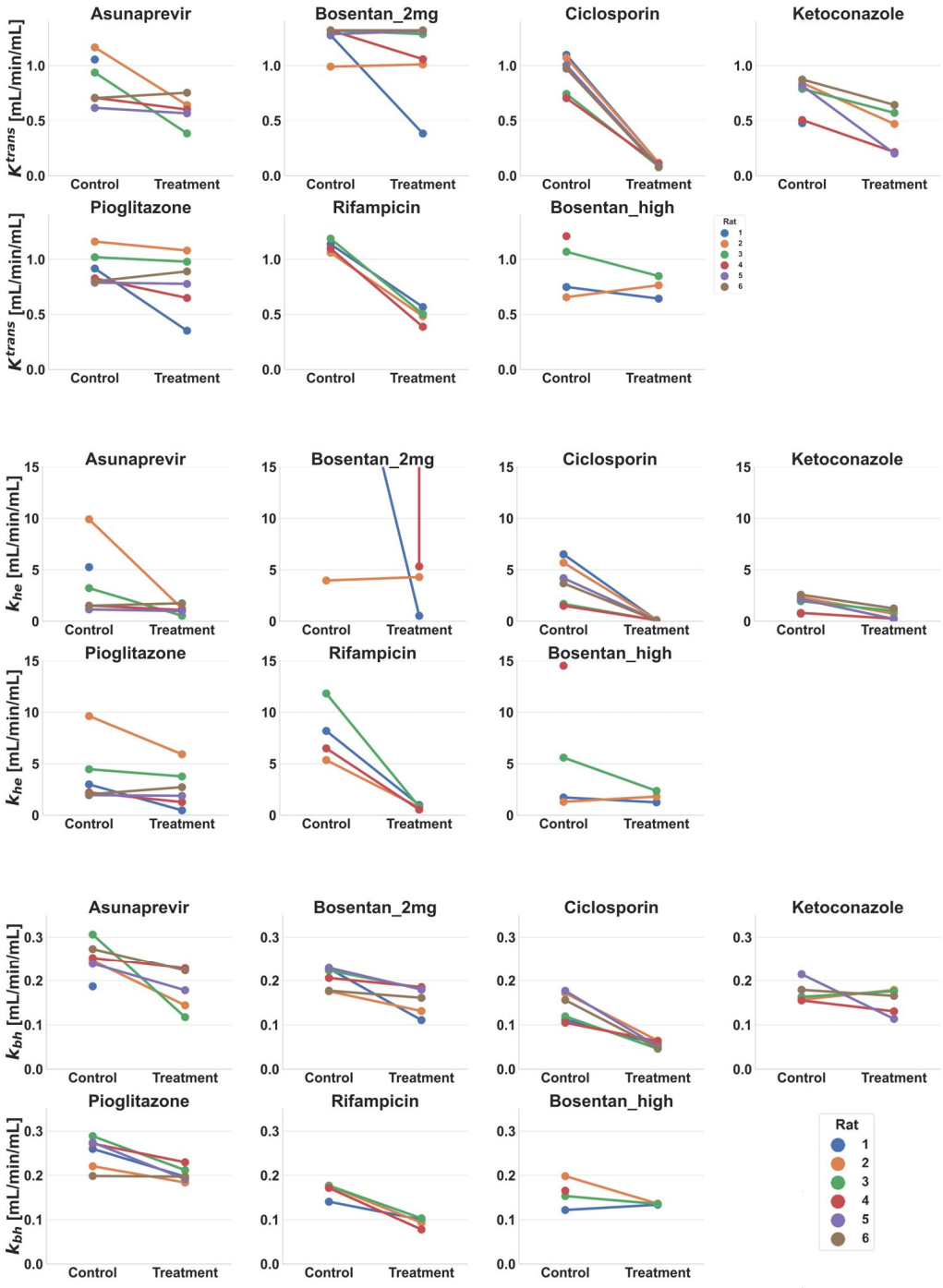

Figure 7. Effect of drug administration on estimated tracer-kinetic model rate constants for hepatic plasma clearance (K^{trans}), hepatic gadoxetate uptake (k_{he}), and biliary excretion (k_{bh}), for different sites (D, E, G1, and G2) and drugs. Each line represents a single rat. Doses for each drug are listed in Table 1, where Bosentan_high refers to the 4–6 mg/kg doses of bosentan.

4. Discussion

A major challenge for prediction of transporter-mediated clinical DDIs is poor translation between in vitro transporter inhibition data and in vivo functional effects. In such instances, plasma DDI data, or interaction data with endogenous biomarkers for transporters of interest, have been used to refine PBPK model parameters [34,56]. However, verification of the predicted changes in tissue exposure as a result of transporter modulation remains a challenge. The current study effectively incorporated modelling and simulation techniques into the design and data analysis of gadoxetate DCE-MRI experiments to enable quantification of the effects of multiple tests-drugs on the function of hepatic OATP1B and MRP2 transporters in vivo (Figure 2).

4.1. Data Analysis and Endpoints for Transporter Interaction Assessment with Imaging Data

The application of imaging modalities for evaluation of tissue exposure and local pharmacokinetic measurement (e.g., in liver, brain, and tumors), has shown promising results [23,57–62]. In the current study, an assessment of drug effects on gadoxetate was performed, using both non-compartmental analysis (i.e., $AUCR$ of ΔR_1 profiles in liver and plasma), and tracer-kinetic modelling. Alternatively, integration plot analysis may be applied for analysis of kinetic imaging data, but this approach has a number of limitations, including (i) the need for imaging data from the bile duct or intestine (not measured in current study), (ii) the very rapid uptake phase of gadoxetate in the liver and elimination from plasma (Figures 3 and 4), and (iii) an inability to differentiate roles of blood flow and transporter activity with respect to hepatic uptake. The tracer-kinetic and PBPK models applied in the current study overcame these limitations.

Assessment of changes in the victim drug AUC ($AUCR$), is a standard endpoint for evaluation of the magnitude of DDI in drug development, representing the net effect of the interaction on the exposure in the plasma [63,64] (Figure 8). $AUCR$ (either clinically observed or predicted by PBPK modelling) is often used to inform dosage adjustment (or contraindication) recommendations for clinical practice, involving the specific pair of co-administered drugs. In the current study, the PBPK predictions of $AUCR$, based on IVIVE of in vitro transporter inhibition data, tended to under-predict the magnitude of gadoxetate interactions when compared with the in vivo data in the liver, but showed reasonable predictive performance for plasma data (Figure 5). A limitation of net-effect parameters, such as plasma or liver $AUCR$, is that the perturbations of specific processes (e.g., uptake and efflux) may not be readily delineated from the analysis of the observed data. In contrast, PBPK and tracer-kinetic modelling of the DCE-MRI data can estimate drugs' effects on both transporters mediated uptake (i.e., k_{he} or CL_{active}) and efflux (k_{bh} or $CL_{biliary}$). As an example, the median decrease in gadoxetate liver AUC, by 74%, was noted in the presence of ciclosporin compared to the control (Table 4). The uptake rate (k_{he}) was estimated to decrease by 96% using the tracer-kinetic model (Table 5), while IVIVE-PBPK simulations predicted between 97% and 98% inhibition of CL_{active} during the gadoxetate DCE-MRI period. Therefore, for the purpose of quantifying the perturbation effects of inhibitor drugs on specific transport processes, model-based analysis of imaging data is recommended.

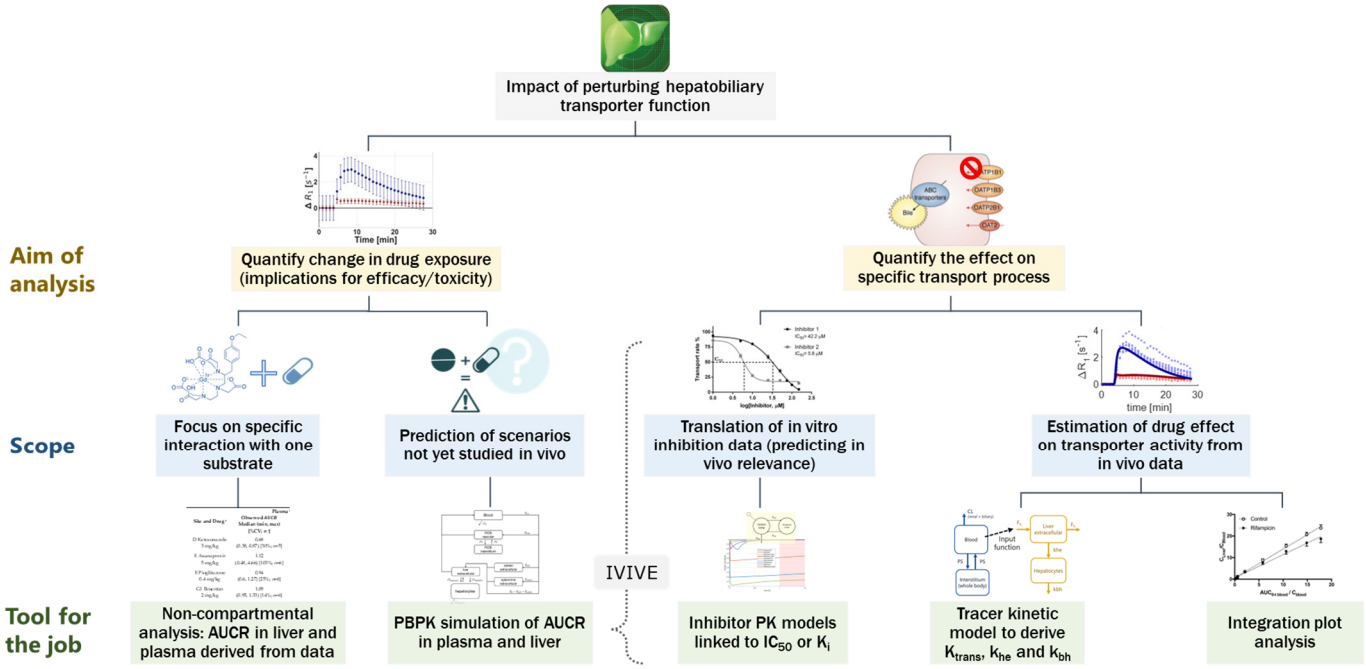

Figure 8. Scheme showing the applications for the data analysis 'toolkit' for quantitative evaluation of perturbations in transporter kinetics from imaging data.

4.2. Integrative Approach Needed to Interpret Imaging Data

In this work, the PBPK model, coupled with the drugs' pharmacokinetic models, predicted the changes in gadoxetate plasma *AUC*, following coadministration of the six drugs investigated in this study, with reasonable accuracy. In the case of liver, the model could distinguish the negative controls from the OATP1B inhibitors. The exception was ketoconazole which caused a decrease in gadoxetate *AUC* compared with control both in plasma (1.5-fold) and in the liver (2-fold). The in vitro OATP1B1 IC_{50} (>2 µM; Table 3) for ketoconazole is relatively high compared with its plasma exposure (unbound C_{max} ~0.07 µM), and hence in vivo inhibition of hepatic uptake transport was not expected for this drug. rNtcp/NTCP was also reported to transport gadoxetate; inhibition of rNtcp by ketoconazole is also unlikely, considering the high IC_{50} for NTCP (202 µM, Table 3). Plausible explanations of the unexpected gadoxetate *AUC* observations with ketoconazole include instrument or signal-to-ΔR_1 errors, an altered volume of interstitial space in the spleen (which was used to derive the plasma DCE-MRI profile) between the two phases of the study, or dosing error in either of the two occasions. An acute dose of ketoconazole is not expected to affect renal function parameters, such as glomerular filtration rate. Although some inhibitory interaction with rOatp4c1 in the kidney (expressed on the apical membrane of rat kidney [65]) could be speculated, there is no evidence to support it. The tracer-kinetic model estimated a 46% decrease in gadoxetate K^{trans} for ketoconazole, and when applied to the extended clearance concept paradigm [66], this decrease in K^{trans} should cause an increase in plasma AUC, the opposite to the observed data. This apparent paradox is likely explained by the use of a population mean two-compartment pharmacokinetic model for gadoxetate as input function for the tracer-kinetic model. As such, in the case of ketoconazole, it is unlikely that the estimated decrease in K^{trans} and k_{he} is reflecting a true inhibition of rOatp1b transporter activity, highlighting the importance of a holistic approach to interpretation of imaging data, considering the interplay of biological and technical systems.

4.3. Biological Relevance of Interaction Effects on K^{trans}, k_{he}, and k_{bh}

Quantifying the effects on uptake and efflux transporters could provide valuable insights into DDI affecting drugs whose pharmacology targets are expressed within hepatocytes, e.g., statins. Insight can also be attained on the effects on bilirubin clearance that are not due to overt liver injury, or inhibition of glucuronidation. When normalized to the same units and reference concentrations, transport rate parameters in the PBPK and tracer-kinetic models were within 4-fold of one another, indicating reasonable consistency at the quantitative level (Table S11). Rifampicin and ciclosporin markedly inhibited gadoxetate uptake activity in vivo, based upon k_{he} in the control and inhibitory phases (Figure 7 and Table 5), in agreement with clinical OATP1B-mediated DDIs [6]. Ketoconazole has well-reported hepatotoxicity [67], but was not expected to result in OATP1B-mediated interaction in vivo [68] (Table 3).

Differentiation of K^{trans} and k_{he} has been overlooked in previous applications of tracer-kinetic modelling of gadoxetate DCE-MRI data in rats [17,27], but was important to consider in the current study, where the aim was to quantify treatment effects on rate constants, and (i) the establish biological relevance of the changes, and (ii) compare these across drugs. In particular, the hepatic extraction ratio (E) for gadoxetate in rats can be high in the absence of drugs (e.g., E > 0.95); in these cases, derived K^{trans} values approach the fixed liver perfusion rate and the system becomes perfusion-limited, making quantitative estimation of drugs' effects on hepatic uptake (k_{he}) highly conditional on the assumed value for liver perfusion. This scenario was evident for the bosentan 2 mg/kg dose, where physiologically implausible values were observed for k_{he}, highlighting the necessity to consider both K^{trans} and k_{he} in data interpretation. The high extraction scenario limits the ability to detect hepatic rOatp1b inhibition in rats for weaker inhibitors. In humans, gadoxetate hepatic extraction is lower than in rats (approx. 20% [20,69,70]), and therefore would be of less concern for gadoxetate-based detection of OATP1B/MRP2-mediated DDIs. It is therefore recommended to consider both K^{trans} and k_{he} when considering the biological relevance of treatment effects on rate constants in rats.

Quantifying the effects on rMrp2 could be especially valuable, since this could result in concentrations of drugs and metabolites within the liver which differ with the ones in plasma [6,59]. For all six drugs investigated here, the largest effects were observed on the inhibition of active uptake. In addition to uptake parameters (K^{trans} and k_{he}), gadoxetate DCE-MRI data, rifampicin and ciclosporin reduced k_{bh}, suggesting inhibition of biliary efflux, while asunapravir and pioglitazone were associated with only reduced k_{bh}. As expected, reduced K^{trans} and k_{he} were associated with decreased gadoxetate liver AUC in the presence of rifampicin and ciclosporin. In contrast, while reduced k_{bh} would be expected to be associated with an increase in liver AUC [59], this was not the case for asunaprevir (31% decrease in k_{bh}, liver $AUCR$ = 1.01) or pioglitazone (19% decrease in k_{bh}, liver $AUCR$ = 1.1).

4.4. Imaging Data to Support PBPK-Based Quantitative Translation

The PBPK modelling predicted well gadoxetate liver and plasma $AUCR$ in the presence of ciclosporin, but under-predicted the liver $AUCR$ in the case of rifampicin, despite a reasonable prediction in plasma (Figure 5). Possible contributing reasons for this mismatch between the plasma and liver predictive performances for rifampicin include, model assumptions such as the relaxivities and the assumption of fast water exchange, a pragmatic approach to translation of in vitro transporter IC_{50} and K_i data for efflux transporters, and the differential sensitivity of each tissue to uptake transporter inhibition.

In vitro measurements of IC_{50} and K_i are highly variable (e.g., Table 3), and are typically higher than corresponding model-based in vivo estimates [34,71]. Such trends are consistent with underestimation of the magnitude of inhibition of CL_{active} and liver $AUCR$ noted for rifampicin (Figure 6B). Likewise, there are limited examples of translation of in vitro inhibition data for hepatobiliary efflux transporters (e.g., MRP2). The assumption that the inhibitory concentration affecting gadoxetate $CL_{biliary}$ was equal to the unbound

drug concentration in plasma, predicted < 25% inhibition of $CL_{biliary}$ using the median ciclosporin in vitro IC_{50} for MRP2 (Figure S11). Although commonly applied, such assumptions for the operating inhibitory concentrations for hepatobiliary efflux transporters have limitations, as these transporters do not face the plasma, highlighting a need for more mechanistic inhibitor models, which was beyond the scope of the current work. Nevertheless, corresponding PBPK predictions of gadoxetate in the presence of ciclosporin were not inconsistent with the observed data, and previous studies suggest that in vivo inhibition of rMrp2/MRP2 by ciclosporin may be modest [30,72]. An attempt to simulate the inhibition of $CL_{biliary}$ using the estimated unbound concentration in the hepatocyte (considering inhibitor liver Kpuu) overestimated the degree of this interaction (75–82% inhibition), based upon the gadoxetate DCE-MRI profile and the analysis using the tracer-kinetic model (59% decrease in k_{bh}) (Figure 7 and Table 5).

In the case of gadoxetate, plasma and liver are expected to have differential sensitivity to rOatp1b2 inhibition. Whereas transporter-mediated uptake is the predominant contributing mechanism to gadoxetate uptake into hepatocytes [23], elimination of gadoxetate from systemic circulation is by both hepatic and renal elimination. As such, the liver *AUC* will be more sensitive to transporter inhibition compared with plasma. It is easier for a PBPK model prediction to appear successful when *AUCR* is close to 1 (e.g., lack of DDI, as in the case of plasma for 2 mg/kg rifampicin) [73]. Therefore, availability of liver imaging data provided further insight into the under-prediction of inhibition of hepatic uptake transport, which could not be obtained by an assessment of the DDI data in plasma alone. This finding reinforces the advantage of the liver imaging data for evaluating predictions of transporter DDIs. Upon translation to the clinical setting, imaging biomarker data can hence facilitate future refinement of PBPK models of hepatobiliary transporter inhibitors, to enhance the current paradigm of using a PBPK-projection of DDI magnitude in untested scenarios to support clinical study design and labelling recommendations [10,63].

5. Conclusions

In the current work, gadoxetate DCE-MRI imaging biomarkers (K^{trans}, k_{he}, and k_{bh}) were demonstrated as promising for the detection and quantification of DDI via rOatp1b/rMrp2, in a preclinical setting, to identify compounds for which clinical DDI studies could be prioritized or deprioritized. Our preclinical studies show the potential to integrate PBPK modelling and tracer-kinetic models of gadoxetate DCE-MRI data in the framework of drug development (Figure 8).

Gadoxetate PBPK models (especially if extended to humans) are useful for translating in vitro transporters' inhibition data of investigational new drugs, and prospective prediction of DDI risks and modulation of liver exposure, in support of other existing modelling tools/biomarkers. In future work, we will test and extend this integrative approach to humans, by analyzing clinical gadoxetate DCE-MRI profiles with both PBPK and tracer-kinetic modelling approaches.

Supplementary Materials: The following supporting information can be downloaded at: https://www.mdpi.com/article/10.3390/pharmaceutics15030896/s1. Supplementary Sections S1–S6. References [74–110] are cited in Supplementary Materials.

Author Contributions: Conceptualization, J.G.K., J.C.W., S.S., G.S. and A.G.; methodology, D.S., J.G.K., C.G., C.D.G.H., I.L., P.D.H., S.S., J.C.W., G.S. and A.G.; software, N.M., D.S., E.R.G. and S.S. formal analysis, N.M., D.S., K.O., E.R.G. and S.S.; investigation, N.M., D.S., C.G., C.D.G.H., I.L., P.D.H., E.R.G. and S.S.; resources, C.D.G.H., I.L., P.D.H., S.S., G.S. and A.G.; data curation, N.M., D.S., C.G., C.D.G.H., I.L., P.D.H., E.R.G. and S.S.; writing—original draft preparation, N.M., D.S., C.G., C.D.G.H., I.L., P.D.H., E.R.G. and S.S.; writing—review and editing, J.G.K., K.O., J.C.W., G.S. and A.G.; visualization, N.M., D.S. and E.R.G.; supervision, J.G.K., C.D.G.H., J.C.W., S.S., G.S. and A.G.; project administration, J.G.K., C.D.G.H. and J.C.W.; funding acquisition, J.G.K., C.D.G.H., I.L., P.D.H., S.S., J.C.W., G.S. and A.G. All authors have read and agreed to the published version of the manuscript.

Funding: The research leading to these results received funding from the Innovative Medicines Initiatives 2 Joint Undertaking under grant agreement No 116106. This Joint Undertaking receives support from the European Union's Horizon 2020 research and innovation programme and EFPIA.

Institutional Review Board Statement: Animal procedures were compliant with directive 2010/63/EU for studies performed in the European Union. All protocols in this study were approved by the Institutional Animal Care and Use Committee at Merck & Co., Inc., Rahway, NJ, USA and were in compliance with the 8th edition Guide for the Care and Use of Laboratory Animals published by the National Research Council (National Academies Press, revised 2011). The protocols were approved by ethics committee (protocol number FH-1022, Regierungspräsidium Darmstadt, Hessen).

Informed Consent Statement: Not applicable.

Data Availability Statement: Data and code presented in this study are openly available in Zenodo, as follows: 1. DCE-MRI datasets and results in CSV format: https://zenodo.org/record/7506968#.Y7cUhNXP1PY; https://doi.org/10.5281/zenodo.7506968 (published on 5 January 2023). 2. Tracer-kinetic model source code archived from GitHub: https://zenodo.org/record/7507642#.Y7cVF9XP1PZ; https://doi.org/10.5281/zenodo.7507642 (published on 5 January 2023). 3. PMI (Platform for research in Medical Imaging) v3.1 software: https://zenodo.org/record/4382479#.Y7cVntXP1PY; https://doi.org/10.5281/zenodo.4382479 (published on 21 December 2020).

Acknowledgments: We are grateful to Katja Hassemer, Ute Thoma, and Nico Zimmer, at Sanofi-Aventis Deutschland Gmbh, for their excellent technical assistance.

Conflicts of Interest: NM, DS, KO, ERG and AG declare no conflict of interest. CG (at the time of work), and GS are employees of Bayer AG, a for-profit company marketing the MR contrast agent gadoxetate, trade name Primovist (Eovist in the USA). SS discloses: PhD studentship co-funding by Bayer. JCW holds stock in Quantitative Imaging Ltd. and is a Director of, and has received compensation from, Bioxydyn Ltd., a for-profit company engaged in the discovery and development of MR biomarkers and the provision of imaging biomarker services. JGK has received compensation from Bioxydyn Ltd., provides fee for consultancy advice to various pharmaceutical companies, and undertakes paid consultancy of Cosmetics Europe, which is the European trade association for the cosmetics and personal care industry. PDH is an employee of Antaros Medical, a for-profit company engaged in the provision of imaging biomarker services. CH was an employee of Merck Sharp & Dohme LLC, a subsidiary of Merck & Co., Inc., Rahway, NJ, USA, and owned stock in Merck & Co., Inc., Rahway, NJ, USA at the time the work was performed and is currently an employee of GSK. IL was an employee of, and received compensation from Sanofi-Aventis Deutschland GmbH at the time the work was performed and is currently an employee of Antaros Medical.

References

1. Neuvonen, P.J.; Niemi, M.; Backman, J.T. Drug interactions with lipid-lowering drugs: Mechanisms and clinical relevance. *Clin. Pharmacol. Ther.* **2006**, *80*, 565–581. [CrossRef] [PubMed]
2. Galetin, A.; Zhao, P.; Huang, S.M. Physiologically Based Pharmacokinetic Modeling of Drug Transporters to Facilitate Individualized Dose Prediction. *J. Pharm. Sci.* **2017**, *106*, 2204–2208. [CrossRef] [PubMed]
3. Zamek-Gliszczynski, M.J.; Chu, X.; Cook, J.A.; Custodio, J.M.; Galetin, A.; Giacomini, K.M.; Lee, C.A.; Paine, M.F.; Ray, A.S.; Ware, J.A.; et al. ITC Commentary on Metformin Clinical Drug-Drug Interaction Study Design That Enables an Efficacy- and Safety-Based Dose Adjustment Decision. *Clin. Pharmacol. Ther.* **2018**, *104*, 781–784. [CrossRef]
4. Taskar, K.S.; Pilla Reddy, V.; Burt, H.; Posada, M.M.; Varma, M.; Zheng, M.; Ullah, M.; Emami Riedmaier, A.; Umehara, K.I.; Snoeys, J.; et al. Physiologically-Based Pharmacokinetic Models for Evaluating Membrane Transporter Mediated Drug-Drug Interactions: Current Capabilities, Case Studies, Future Opportunities, and Recommendations. *Clin. Pharmacol. Ther.* **2020**, *107*, 1082–1115. [CrossRef] [PubMed]
5. Yoshida, K.; Zhao, P.; Zhang, L.; Abernethy, D.R.; Rekic, D.; Reynolds, K.S.; Galetin, A.; Huang, S.M. In Vitro-In Vivo Extrapolation of Metabolism- and Transporter-Mediated Drug-Drug Interactions-Overview of Basic Prediction Methods. *J. Pharm. Sci.* **2017**, *106*, 2209–2213. [CrossRef]
6. Guo, Y.; Chu, X.; Parrott, N.J.; Brouwer, K.L.R.; Hsu, V.; Nagar, S.; Matsson, P.; Sharma, P.; Snoeys, J.; Sugiyama, Y.; et al. Advancing Predictions of Tissue and Intracellular Drug Concentrations Using In Vitro, Imaging and Physiologically Based Pharmacokinetic Modeling Approaches. *Clin. Pharmacol. Ther.* **2018**, *104*, 865–889. [CrossRef]
7. Grimstein, M.; Yang, Y.; Zhang, X.; Grillo, J.; Huang, S.M.; Zineh, I.; Wang, Y. Physiologically Based Pharmacokinetic Modeling in Regulatory Science: An Update From the U.S. Food and Drug Administration's Office of Clinical Pharmacology. *J. Pharm. Sci.* **2019**, *108*, 21–25. [CrossRef]

8. Snyder, E.; Banks, K.P. Hepatobiliary Scintigraphy. In *StatPearls*; StatPearls Publishing LLC.: Treasure Island, FL, USA, 2022.
9. US Food Drug Admin. Physiologically Based Pharmacokinetic Analyses—Format and Content: Guidance for Industry; Silver Spring, MD, USA, 2018. 2018. Available online: https://www.fda.gov/media/101469/download (accessed on 1 March 2023).
10. The International Council for Harmonisation of Technical Requirements for Pharmaceuticals for Human Use. ICH Harmonised Guidline M12 Drug Interaction Studies [Draft Version]. Geneva, Switzerland, 2022. Available online: https://www.ema.europa.eu/en/documents/scientific-guideline/draft-ich-guideline-m12-drug-interaction-studies-step-2b_en.pdf (accessed on 1 March 2023).
11. Billington, S.; Shoner, S.; Lee, S.; Clark-Snustad, K.; Pennington, M.; Lewis, D.; Muzi, M.; Rene, S.; Lee, J.; Nguyen, T.B.; et al. Positron Emission Tomography Imaging of [(11) C]Rosuvastatin Hepatic Concentrations and Hepatobiliary Transport in Humans in the Absence and Presence of Cyclosporin A. *Clin. Pharmacol. Ther.* **2019**, *106*, 1056–1066. [CrossRef]
12. Levesque, E.; Martin, E.; Dudau, D.; Lim, C.; Dhonneur, G.; Azoulay, D. Current use and perspective of indocyanine green clearance in liver diseases. *Anaesth. Crit. Care Pain Med.* **2016**, *35*, 49–57. [CrossRef]
13. Lu, H.; Clingman, C.; Golay, X.; van Zijl, P.C. Determining the longitudinal relaxation time (T1) of blood at 3.0 Tesla. *Magn. Reson. Med.* **2004**, *52*, 679–682. [CrossRef]
14. US Food Drug Admin. Drug Labeling-Package Insert: EOVIST (Gadoxetate Disodium) Injection [FDA Application No, (NDA) 022090]. 2018. Available online: https://www.accessdata.fda.gov/drugsatfda_docs/label/2018/022090s016lbl.pdf (accessed on 5 April 2019).
15. Sourbron, S.P.; Buckley, D.L. Classic models for dynamic contrast-enhanced MRI. *NMR Biomed.* **2013**, *26*, 1004–1027. [CrossRef] [PubMed]
16. Sourbron, S.; Sommer, W.H.; Reiser, M.F.; Zech, C.J. Combined quantification of liver perfusion and function with dynamic gadoxetic acid-enhanced MR imaging. *Radiology* **2012**, *263*, 874–883. [CrossRef]
17. Karageorgis, A.; Lenhard, S.C.; Yerby, B.; Forsgren, M.F.; Liachenko, S.; Johansson, E.; Pilling, M.A.; Peterson, R.A.; Yang, X.; Williams, D.P.; et al. A multi-center preclinical study of gadoxetate DCE-MRI in rats as a biomarker of drug induced inhibition of liver transporter function. *PLoS ONE* **2018**, *13*, e0197213. [CrossRef] [PubMed]
18. Giraudeau, C.; Leporq, B.; Doblas, S.; Lagadec, M.; Pastor, C.M.; Daire, J.L.; Van Beers, B.E. Gadoxetate-enhanced MR imaging and compartmental modelling to assess hepatocyte bidirectional transport function in rats with advanced liver fibrosis. *Eur. Radiol.* **2017**, *27*, 1804–1811. [CrossRef]
19. Forsgren, M.F.; Dahlqvist Leinhard, O.; Dahlstrom, N.; Cedersund, G.; Lundberg, P. Physiologically realistic and validated mathematical liver model reveals [corrected] hepatobiliary transfer rates for Gd-EOB-DTPA using human DCE-MRI data. *PLoS ONE* **2014**, *9*, e95700. [CrossRef] [PubMed]
20. Georgiou, L.; Penny, J.; Nicholls, G.; Woodhouse, N.; Ble, F.X.; Hubbard Cristinacce, P.L.; Naish, J.H. Quantitative Assessment of Liver Function Using Gadoxetate-Enhanced Magnetic Resonance Imaging: Monitoring Transporter-Mediated Processes in Healthy Volunteers. *Investig. Radiol.* **2017**, *52*, 111–119. [CrossRef]
21. Spanakis, M.; Marias, K. In silico evaluation of gadofosveset pharmacokinetics in different population groups using the Simcyp® simulator platform. *Silico Pharm.* **2014**, *2*, 2. [CrossRef]
22. Spanakis, M.; Kontopodis, E.; Van Cauter, S.; Sakkalis, V.; Marias, K. Assessment of DCE-MRI parameters for brain tumors through implementation of physiologically-based pharmacokinetic model approaches for Gd-DOTA. *J. Pharmacokinet. Pharmacodyn.* **2016**, *43*, 529–547. [CrossRef]
23. Scotcher, D.; Melillo, N.; Tadimalla, S.; Darwich, A.S.; Ziemian, S.; Ogungbenro, K.; Schutz, G.; Sourbron, S.; Galetin, A. Physiologically Based Pharmacokinetic Modeling of Transporter-Mediated Hepatic Disposition of Imaging Biomarker Gadoxetate in Rats. *Mol. Pharm.* **2021**, *18*, 2997–3009. [CrossRef]
24. Green, C.; Tadimalla, S.; Steinmann, D.; Sourbron, S.; Koehler, S.; Juretschke, H.-P.; Laitinen, I.; Waterton, J.C.; Hockings, P.D.; Hines, C.D.G.; et al. Inter-site repeatability and quantitative assessment of hepatic transporter function with DCE-MRI in rats [Abstract #1773]. In Proceedings of the ISMRM 27th Annual Meeting and Exhibition, Montreal, QC, Canada, 11–16 May 2019.
25. Waterton, J.C.; Hines, C.D.G.; Hockings, P.D.; Laitinen, I.; Ziemian, S.; Campbell, S.; Gottschalk, M.; Green, C.; Haase, M.; Hassemer, K.; et al. Repeatability and reproducibility of longitudinal relaxation rate in 12 small-animal MRI systems. *Magn. Reson. Imaging* **2019**, *59*, 121–129. [CrossRef]
26. Schuhmann-Giampieri, G.; Schmitt-Willich, H.; Press, W.R.; Negishi, C.; Weinmann, H.J.; Speck, U. Preclinical evaluation of Gd-EOB-DTPA as a contrast agent in MR imaging of the hepatobiliary system. *Radiology* **1992**, *183*, 59–64. [CrossRef]
27. Ulloa, J.L.; Stahl, S.; Yates, J.; Woodhouse, N.; Kenna, J.G.; Jones, H.B.; Waterton, J.C.; Hockings, P.D. Assessment of gadoxetate DCE-MRI as a biomarker of hepatobiliary transporter inhibition. *NMR Biomed.* **2013**, *26*, 1258–1270. [CrossRef]
28. Sourbron, S. *Plaresmedima/PMI-0.4-TRISTAN-RATS: TRISTAN RATS v3.1 (v3.1)*; Zenodo: Genève, Switzerland, 2020. [CrossRef]
29. Gertz, M.; Tsamandouras, N.; Sall, C.; Houston, J.B.; Galetin, A. Reduced physiologically-based pharmacokinetic model of repaglinide: Impact of OATP1B1 and CYP2C8 genotype and source of in vitro data on the prediction of drug-drug interaction risk. *Pharm. Res.* **2014**, *31*, 2367–2382. [CrossRef]
30. Gertz, M.; Cartwright, C.M.; Hobbs, M.J.; Kenworthy, K.E.; Rowland, M.; Houston, J.B.; Galetin, A. Cyclosporine inhibition of hepatic and intestinal CYP3A4, uptake and efflux transporters: Application of PBPK modeling in the assessment of drug-drug interaction potential. *Pharm. Res.* **2013**, *30*, 761–780. [CrossRef]
31. Sourbron, S. Technical aspects of MR perfusion. *Eur. J. Radiol.* **2010**, *76*, 304–313. [CrossRef]

32. Ziemian, S.; Green, C.; Sourbron, S.; Jost, G.; Schütz, G.; Hines, C.D.G. Ex vivo gadoxetate relaxivities in rat liver tissue and blood at five magnetic field strengths from 1.41 to 7 T. *NMR Biomed.* **2021**, *34*, e4401. [CrossRef]
33. Gunwhy, E.; Sourbron, S. *TRISTAN-Rat (v1.0.0)*; Zenodo: Genève, Switzerland, 2023. [CrossRef]
34. Barnett, S.; Ogungbenro, K.; Menochet, K.; Shen, H.; Lai, Y.; Humphreys, W.G.; Galetin, A. Gaining Mechanistic Insight Into Coproporphyrin I as Endogenous Biomarker for OATP1B-Mediated Drug-Drug Interactions Using Population Pharmacokinetic Modeling and Simulation. *Clin. Pharmacol. Ther.* **2018**, *104*, 564–574. [CrossRef]
35. Lau, Y.Y.; Okochi, H.; Huang, Y.; Benet, L.Z. Multiple transporters affect the disposition of atorvastatin and its two active hydroxy metabolites: Application of in vitro and ex situ systems. *J. Pharmacol. Exp. Ther.* **2006**, *316*, 762–771. [CrossRef]
36. Ishida, K.; Ullah, M.; Tóth, B.; Juhasz, V.; Unadkat, J.D. Transport Kinetics, Selective Inhibition, and Successful Prediction of In Vivo Inhibition of Rat Hepatic Organic Anion Transporting Polypeptides. *Drug Metab. Dispos.* **2018**, *46*, 1251–1258. [CrossRef]
37. Nakanishi, T.; Shibue, Y.; Fukuyama, Y.; Yoshida, K.; Fukuda, H.; Shirasaka, Y.; Tamai, I. Quantitative time-lapse imaging-based analysis of drug-drug interaction mediated by hepatobiliary transporter, multidrug resistance-associated protein 2, in sandwich-cultured rat hepatocytes. *Drug Metab. Dispos.* **2011**, *39*, 984–991. [CrossRef]
38. Shitara, Y.; Sugiyama, D.; Kusuhara, H.; Kato, Y.; Abe, T.; Meier, P.J.; Itoh, T.; Sugiyama, Y. Comparative inhibitory effects of different compounds on rat oatpl (slc21a1)- and Oatp2 (Slc21a5)-mediated transport. *Pharm. Res.* **2002**, *19*, 147–153. [CrossRef]
39. Shitara, Y.; Hirano, M.; Adachi, Y.; Itoh, T.; Sato, H.; Sugiyama, Y. In vitro and in vivo correlation of the inhibitory effect of cyclosporin A on the transporter-mediated hepatic uptake of cerivastatin in rats. *Drug Metab. Dispos.* **2004**, *32*, 1468–1475. [CrossRef]
40. Tang, W.; Stearns, R.A.; Chen, Q.; Bleasby, K.; Teffera, Y.; Colletti, A.; Hafey, M.; Evers, R.; Dean, D.C.; Magriotis, P.A.; et al. Importance of mechanistic drug metabolism studies in support of drug discovery: A case study with an N -sulfonylated dipeptide VLA-4 antagonist in rats. *Xenobiotica* **2008**, *38*, 223–237. [CrossRef] [PubMed]
41. Li, Y.; Evers, R.; Hafey, M.J.; Cheon, K.; Duong, H.; Lynch, D.; LaFranco-Scheuch, L.; Pacchione, S.; Tamburino, A.M.; Tanis, K.Q.; et al. Use of a Bile Salt Export Pump Knockdown Rat Susceptibility Model to Interrogate Mechanism of Drug-Induced Liver Toxicity. *Toxicol. Sci.* **2019**, *170*, 180–198. [CrossRef] [PubMed]
42. Barber, J.A.; Stahl, S.H.; Summers, C.; Barrett, G.; Park, B.K.; Foster, J.R.; Kenna, J.G. Quantification of Drug-Induced Inhibition of Canalicular Cholyl-l-Lysyl-Fluorescein Excretion from Hepatocytes by High Content Cell Imaging. *Toxicol. Sci.* **2015**, *148*, 48–59. [CrossRef] [PubMed]
43. McPhee, F.; Sheaffer, A.K.; Friborg, J.; Hernandez, D.; Falk, P.; Zhai, G.; Levine, S.; Chaniewski, S.; Yu, F.; Barry, D.; et al. Preclinical Profile and Characterization of the Hepatitis C Virus NS3 Protease Inhibitor Asunaprevir (BMS-650032). *Antimicrob. Agents Chemother.* **2012**, *56*, 5387–5396. [CrossRef]
44. Dingemanse, J.; van Giersbergen, P.L. Clinical pharmacology of bosentan, a dual endothelin receptor antagonist. *Clin. Pharmacokinet.* **2004**, *43*, 1089–1115. [CrossRef]
45. Pedersen, J.M.; Matsson, P.; Bergstrom, C.A.; Norinder, U.; Hoogstraate, J.; Artursson, P. Prediction and identification of drug interactions with the human ATP-binding cassette transporter multidrug-resistance associated protein 2 (MRP2; ABCC2). *J. Med. Chem.* **2008**, *51*, 3275–3287. [CrossRef]
46. Vermeer, L.M.; Isringhausen, C.D.; Ogilvie, B.W.; Buckley, D.B. Evaluation of Ketoconazole and Its Alternative Clinical CYP3A4/5 Inhibitors as Inhibitors of Drug Transporters: The In Vitro Effects of Ketoconazole, Ritonavir, Clarithromycin, and Itraconazole on 13 Clinically-Relevant Drug Transporters. *Drug Metab. Dispos.* **2016**, *44*, 453–459. [CrossRef]
47. Morgan, R.E.; van Staden, C.J.; Chen, Y.; Kalyanaraman, N.; Kalanzi, J.; Dunn, R.T., 2nd; Afshari, C.A.; Hamadeh, H.K. A multifactorial approach to hepatobiliary transporter assessment enables improved therapeutic compound development. *Toxicol. Sci.* **2013**, *136*, 216–241. [CrossRef]
48. Gillies, P.S.; Dunn, C.J. Pioglitazone. *Drugs* **2000**, *60*, 333–343. [CrossRef]
49. Hachad, H.; Ragueneau-Majlessi, I.; Levy, R.H. A useful tool for drug interaction evaluation: The University of Washington Metabolism and Transport Drug Interaction Database. *Hum. Genom.* **2010**, *5*, 61–72. [CrossRef]
50. US Food Drug Admin. Drug Labeling-Package Insert: RIFADIN®(Rifampin Capsules USP) and RIFADIN®IV (Rifampin for Injection USP) [FDA Application No, (NDA) #050627]. 2022. Available online: https://www.accessdata.fda.gov/drugsatfda_docs/label/2022/050420s087,050627s030lbl.pdf (accessed on 1 July 2022).
51. Australia Therapeutic Goods Administration. Product Information for AusPAR Sunvepra Asunaprevir. 2015. Available online: https://www.tga.gov.au/sites/default/files/auspar-asunaprevir-151214-pi.pdf (accessed on 1 July 2022).
52. US Food Drug Admin. Drug Labeling-Package Insert: TRACLEER®(Bosentan) Tablets, for Oral Use TRACLEER®(Bosentan) Tablets for Oral Suspension [FDA Application No, (NDA) #209279]. 2017. Available online: www.accessdata.fda.gov/drugsatfda_docs/label/2017/209279s000lbl.pdf (accessed on 1 July 2022).
53. US Food Drug Admin. Drug Labeling-Package Insert: NEORAL(Cyclosporine) Capsules and Oral Solution [FDA Application No, (NDA) 050715]. 2009. Available online: https://www.accessdata.fda.gov/drugsatfda_docs/label/2009/050715s027,050716s028lbl.pdf (accessed on 1 March 2022).
54. US Food Drug Admin. Drug Labeling-Package Insert: Sandimmune®Soft Gelatin Capsules (Cyclosporine Capsules, USP) Sandimmune®Oral Solution (Cyclosporine Oral Solution, USP) Sandimmune®Injection (Cyclosporine Injection, USP) [FDA Application no, (NDA) 050573]. 2015. Available online: https://www.accessdata.fda.gov/drugsatfda_docs/label/2015/050573s041,050574s051,050625s055lbl.pdf (accessed on 1 July 2022).

55. US Food Drug Admin. Drug Labeling-Package Insert: ACTOS (Pioglitazone) Tablets for Oral Use [FDA Application No, (NDA) 021073]. 2016. Available online: www.accessdata.fda.gov/drugsatfda_docs/label/2017/021073s049lbl.pdf (accessed on 1 July 2022).
56. Kimoto, E.; Costales, C.; West, M.A.; Bi, Y.A.; Vourvahis, M.; David Rodrigues, A.; Varma, M.V.S. Biomarker-Informed Model-Based Risk Assessment of Organic Anion Transporting Polypeptide 1B Mediated Drug-Drug Interactions. *Clin. Pharmacol. Ther.* **2022**, *111*, 404–415. [CrossRef] [PubMed]
57. Sasongko, L.; Link, J.M.; Muzi, M.; Mankoff, D.A.; Yang, X.; Collier, A.C.; Shoner, S.C.; Unadkat, J.D. Imaging P-glycoprotein transport activity at the human blood-brain barrier with positron emission tomography. *Clin. Pharmacol. Ther.* **2005**, *77*, 503–514. [CrossRef] [PubMed]
58. Takashima, T.; Kitamura, S.; Wada, Y.; Tanaka, M.; Shigihara, Y.; Ishii, H.; Ijuin, R.; Shiomi, S.; Nakae, T.; Watanabe, Y.; et al. PET imaging-based evaluation of hepatobiliary transport in humans with (15R)-11C-TIC-Me. *J. Nucl. Med.* **2012**, *53*, 741–748. [CrossRef]
59. Pfeifer, N.D.; Goss, S.L.; Swift, B.; Ghibellini, G.; Ivanovic, M.; Heizer, W.D.; Gangarosa, L.M.; Brouwer, K.L. Effect of Ritonavir on (99m)Technetium-Mebrofenin Disposition in Humans: A Semi-PBPK Modeling and In Vitro Approach to Predict Transporter-Mediated DDIs. *CPT Pharmacomet. Syst. Pharm.* **2013**, *2*, e20. [CrossRef] [PubMed]
60. Hernández Lozano, I.; Langer, O. Use of imaging to assess the activity of hepatic transporters. *Expert Opin. Drug Metab. Toxicol.* **2020**, *16*, 149–164. [CrossRef] [PubMed]
61. Kenna, J.G.; Waterton, J.C.; Baudy, A.; Galetin, A.; Hines, C.D.G.; Hockings, P.; Patel, M.; Scotcher, D.; Sourbron, S.; Ziemian, S.; et al. Noninvasive Preclinical and Clinical Imaging of Liver Transporter Function Relevant to Drug-Induced Liver Injury. In *Drug-Induced Liver Toxicity*; Chen, M., Will, Y., Eds.; Springer: New York, NY, USA, 2018; pp. 627–651.
62. Slobbe, P.; Windhorst, A.D.; Stigter-van Walsum, M.; Smit, E.F.; Niessen, H.G.; Solca, F.; Stehle, G.; van Dongen, G.A.; Poot, A.J. A comparative PET imaging study with the reversible and irreversible EGFR tyrosine kinase inhibitors [(11)C]erlotinib and [(18)F]afatinib in lung cancer-bearing mice. *EJNMMI Res.* **2015**, *5*, 14. [CrossRef]
63. US Food Drug Admin. *Clinical Drug Interaction Studies—Cytochrome P450 Enzyme- and Transporter-Mediated Drug Interactions Guidance for Industry*; U.S. Food and Drug Administration: Silver Spring, MD, USA, 2020. Available online: https://www.fda.gov/media/134581/download (accessed on 1 March 2022).
64. US Food Drug Admin. In Vitro Drug Interaction Studies—Cytochrome P450 Enzyme- and Transporter-Mediated Drug Interactions Guidance for Industry. U.S. Food and Drug Administration: Silver Spring, MD, USA, 2020. Available online: https://www.fda.gov/media/134582/download (accessed on 1 March 2022).
65. Kuo, K.-L.; Zhu, H.; McNamara, P.J.; Leggas, M. Localization and functional characterization of the rat Oatp4c1 transporter in an in vitro cell system and rat tissues. *PLoS ONE* **2012**, *7*, e39641. [CrossRef]
66. Varma, M.V.; Steyn, S.J.; Allerton, C.; El-Kattan, A.F. Predicting Clearance Mechanism in Drug Discovery: Extended Clearance Classification System (ECCS). *Pharm. Res.* **2015**, *32*, 3785–3802. [CrossRef]
67. Greenblatt, H.K.; Greenblatt, D.J. Liver injury associated with ketoconazole: Review of the published evidence. *J. Clin. Pharmacol.* **2014**, *54*, 1321–1329. [CrossRef] [PubMed]
68. Choi, M.K.; Jin, Q.R.; Choi, Y.L.; Ahn, S.H.; Bae, M.A.; Song, I.S. Inhibitory effects of ketoconazole and rifampin on OAT1 and OATP1B1 transport activities: Considerations on drug-drug interactions. *Biopharm. Drug Dispos.* **2011**, *32*, 175–184. [CrossRef]
69. Weiss, M.; Siegmund, W. Unusual Distribution Kinetics of Gadoxetate in Healthy Human Subjects Genotyped for OATP1B1: Application of Population Analysis and a Minimal Physiological-Based Pharmacokinetic Model. *J. Clin. Pharmacol.* **2021**, *61*, 506–514. [CrossRef]
70. Nilsson, H.; Nordell, A.; Vargas, R.; Douglas, L.; Jonas, E.; Blomqvist, L. Assessment of hepatic extraction fraction and input relative blood flow using dynamic hepatocyte-specific contrast-enhanced MRI. *J. Magn. Reson. Imaging* **2009**, *29*, 1323–1331. [CrossRef]
71. Yoshida, K.; Guo, C.; Sane, R. Quantitative Prediction of OATP-Mediated Drug-Drug Interactions With Model-Based Analysis of Endogenous Biomarker Kinetics. *CPT Pharmacomet. Syst. Pharm.* **2018**, *7*, 517–524. [CrossRef]
72. Westley, I.S.; Brogan, L.R.; Morris, R.G.; Evans, A.M.; Sallustio, B.C. Role of Mrp2 in the hepatic disposition of mycophenolic acid and its glucuronide metabolites: Effect of cyclosporine. *Drug Metab. Dispos.* **2006**, *34*, 261–266. [CrossRef] [PubMed]
73. Guest, E.J.; Aarons, L.; Houston, J.B.; Rostami-Hodjegan, A.; Galetin, A. Critique of the two-fold measure of prediction success for ratios: Application for the assessment of drug-drug interactions. *Drug Metab. Dispos.* **2011**, *39*, 170–173. [CrossRef]
74. Lau, Y.Y.; Okochi, H.; Huang, Y.; Benet, L.Z. Pharmacokinetics of atorvastatin and its hydroxy metabolites in rats and the effects of concomitant rifampicin single doses: Relevance of first-pass effect from hepatic uptake transporters, and intestinal and hepatic metabolism. *Drug Metab. Dispos.* **2006**, *34*, 1175–1181. [CrossRef] [PubMed]
75. Jiang, R.; Dong, J.; Li, X.; Du, F.; Jia, W.; Xu, F.; Wang, F.; Yang, J.; Niu, W.; Li, C. Molecular mechanisms governing different pharmacokinetics of ginsenosides and potential for ginsenoside-perpetrated herb-drug interactions on OATP1B3. *Br. J. Pharmacol.* **2015**, *172*, 1059–1073. [CrossRef]
76. Mosure, K.W.; Knipe, J.O.; Browning, M.; Arora, V.; Shu, Y.Z.; Phillip, T.; McPhee, F.; Scola, P.; Balakrishnan, A.; Soars, M.G.; et al. Preclinical Pharmacokinetics and In Vitro Metabolism of Asunaprevir (BMS-650032), a Potent Hepatitis C Virus NS3 Protease Inhibitor. *J. Pharm. Sci.* **2015**, *104*, 2813–2823. [CrossRef]
77. Kawai, R.; Mathew, D.; Tanaka, C.; Rowland, M. Physiologically based pharmacokinetics of cyclosporine A: Extension to tissue distribution kinetics in rats and scale-up to human. *J. Pharmacol. Exp. Ther.* **1998**, *287*, 457–468. [PubMed]

78. Lindberg-Freijs, A.; Karlsson, M.O. Dose dependent absorption and linear disposition of cyclosporin A in rat. *Biopharm. Drug Dispos.* **1994**, *15*, 75–86. [CrossRef]
79. Fujita, Y.; Yamada, Y.; Kusama, M.; Yamauchi, T.; Kamon, J.; Kadowaki, T.; Iga, T. Sex differences in the pharmacokinetics of pioglitazone in rats. *Comp. Biochem. Physiol. C Toxicol. Pharmacol.* **2003**, *136*, 85–94. [CrossRef]
80. Maeshiba, Y.; Kiyota, Y.; Yamashita, K.; Yoshimura, Y.; Motohashi, M.; Tanayama, S. Disposition of the new antidiabetic agent pioglitazone in rats, dogs, and monkeys. *Arzneimittelforschung* **1997**, *47*, 29–35.
81. Umathe, S.N.; Dixit, P.V.; Kumar, V.; Bansod, K.U.; Wanjari, M.M. Quercetin pretreatment increases the bioavailability of pioglitazone in rats: Involvement of CYP3A inhibition. *Biochem. Pharmacol.* **2008**, *75*, 1670–1676. [CrossRef] [PubMed]
82. Treiber, A.; Schneiter, R.; Delahaye, S.; Clozel, M. Inhibition of organic anion transporting polypeptide-mediated hepatic uptake is the major determinant in the pharmacokinetic interaction between bosentan and cyclosporin A in the rat. *J. Pharmacol. Exp. Ther.* **2004**, *308*, 1121–1129. [CrossRef]
83. Li, R.; Niosi, M.; Johnson, N.; Tess, D.A.; Kimoto, E.; Lin, J.; Yang, X.; Riccardi, K.A.; Ryu, S.; El-Kattan, A.F.; et al. A Study on Pharmacokinetics of Bosentan with Systems Modeling, Part 1: Translating Systemic Plasma Concentration to Liver Exposure in Healthy Subjects. *Drug Metab. Dispos.* **2018**, *46*, 346–356. [CrossRef]
84. Francis, L.J.; Houston, J.B.; Hallifax, D. Impact of Plasma Protein Binding in Drug Clearance Prediction: A Data Base Analysis of Published Studies and Implications for In Vitro-In Vivo Extrapolation. *Drug Metab. Dispos.* **2021**, *49*, 188–201. [CrossRef]
85. Barnett, S.; Ogungbenro, K.; Ménochet, K.; Shen, H.; Humphreys, W.G.; Galetin, A. Comprehensive Evaluation of the Utility of 20 Endogenous Molecules as Biomarkers of OATP1B Inhibition Compared with Rosuvastatin and Coproporphyrin I. *J. Pharmacol. Exp. Ther.* **2019**, *368*, 125–135. [CrossRef]
86. US Food Drug Admin. Drug Development and Drug Interactions: Table of Substrates, Inhibitors and Inducers. Available online: https://www.fda.gov/drugs/drug-interactions-labeling/drug-development-and-drug-interactions-table-substrates-inhibitors-and-inducers (accessed on 18 March 2022).
87. Rifampin. *LiverTox: Clinical and Research Information on Drug-Induced Liver Injury*; National Institute of Diabetes and Digestive and Kidney Diseases: Bethesda, MD, USA, 2012.
88. Abulfathi, A.A.; Decloedt, E.H.; Svensson, E.M.; Diacon, A.H.; Donald, P.; Reuter, H. Clinical Pharmacokinetics and Pharmacodynamics of Rifampicin in Human Tuberculosis. *Clin. Pharmacokinet.* **2019**, *58*, 1103–1129. [CrossRef]
89. Eley, T.; Han, Y.H.; Huang, S.P.; He, B.; Li, W.; Bedford, W.; Stonier, M.; Gardiner, D.; Sims, K.; Rodrigues, A.D.; et al. Organic anion transporting polypeptide-mediated transport of, and inhibition by, asunaprevir, an inhibitor of hepatitis C virus NS3 protease. *Clin. Pharmacol. Ther.* **2015**, *97*, 159–166. [CrossRef] [PubMed]
90. Miyashima, Y.; Honma, Y.; Miyagawa, K.; Oe, S.; Senju, M.; Shibata, M.; Hiura, M.; Abe, S.; Harada, M. Daclatasvir and Asunaprevir Combination Therapy-induced Hepatitis and Cholecystitis with Coagulation Disorder due to Hypersensitivity Reactions. *Intern. Med.* **2016**, *55*, 3595–3601. [CrossRef]
91. Eley, T.; Sevinsky, H.; Huang, S.P.; He, B.; Zhu, K.; Kandoussi, H.; Gardiner, D.; Grasela, D.M.; Bertz, R.; Bifano, M. The pharmacokinetics of daclatasvir and asunaprevir administered in combination in studies in healthy subjects and patients infected with hepatitis C virus. *Clin. Drug Investig.* **2014**, *34*, 661–671. [CrossRef] [PubMed]
92. Duan, P.; Zhao, P.; Zhang, L. Physiologically Based Pharmacokinetic (PBPK) Modeling of Pitavastatin and Atorvastatin to Predict Drug-Drug Interactions (DDIs). *Eur. J. Drug Metab. Pharmacokinet.* **2017**, *42*, 689–705. [CrossRef]
93. Reuben, A. Chapter 31—Hepatotoxicity of Immunosuppressive Drugs. In *Drug-Induced Liver Disease*, 3rd ed.; Kaplowitz, N., DeLeve, L.D., Eds.; Academic Press: Boston, MA, USA, 2013; pp. 569–591.
94. Tanaka, C.; Kawai, R.; Rowland, M. Dose-dependent pharmacokinetics of cyclosporin A in rats: Events in tissues. *Drug Metab. Dispos.* **2000**, *28*, 582–589.
95. Matthew, D.; Brennan, B.; Zomorodi, K.; Houston, J.B. Disposition of azole antifungal agents. I. Nonlinearities in ketoconazole clearance and binding in rat liver. *Pharm. Res.* **1993**, *10*, 418–422. [CrossRef]
96. Daneshmend, T.K.; Warnock, D.W.; Ene, M.D.; Johnson, E.M.; Parker, G.; Richardson, M.D.; Roberts, C.J. Multiple dose pharmacokinetics of ketoconazole and their effects on antipyrine kinetics in man. *J. Antimicrob. Chemother.* **1983**, *12*, 185–188. [CrossRef] [PubMed]
97. Marcy, T.R.; Britton, M.L.; Blevins, S.M. Second-generation thiazolidinediones and hepatotoxicity. *Ann. Pharmacother.* **2004**, *38*, 1419–1423. [CrossRef]
98. Chen, M.; Zhang, J.; Wang, Y.; Liu, Z.; Kelly, R.; Zhou, G.; Fang, H.; Borlak, J.; Tong, W. The liver toxicity knowledge base: A systems approach to a complex end point. *Clin. Pharmacol. Ther.* **2013**, *93*, 409–412. [CrossRef]
99. U.S. Food and Drug Administration. *Clinical Pharmacology and Biopharmaceutics Review*; ACTOS (Pioglitazone Hydrochloride) [FDA Application No, (NDA)021073]; U.S. Food and Drug Administration: Silver Spring, MD, USA, 1999.
100. Eriksson, C.; Gustavsson, A.; Kronvall, T.; Tysk, C. Hepatotoxicity by bosentan in a patient with portopulmonary hypertension: A case-report and review of the literature. *J. Gastrointestin. Liver Dis.* **2011**, *20*, 77–80.
101. Scotcher, D.; Jones, C.R.; Galetin, A.; Rostami-Hodjegan, A. Delineating the Role of Various Factors in Renal Disposition of Digoxin through Application of Physiologically Based Kidney Model to Renal Impairment Populations. *J. Pharmacol. Exp. Ther.* **2017**, *360*, 484–495. [CrossRef] [PubMed]

102. Scotcher, D.; Arya, V.; Yang, X.; Zhao, P.; Zhang, L.; Huang, S.M.; Rostami-Hodjegan, A.; Galetin, A. Mechanistic Models as Framework for Understanding Biomarker Disposition: Prediction of Creatinine-Drug Interactions. *CPT Pharmacomet. Syst. Pharmacol.* **2020**, *9*, 282–293. [CrossRef] [PubMed]
103. Asaumi, R.; Nunoya, K.I.; Yamaura, Y.; Taskar, K.S.; Sugiyama, Y. Robust physiologically based pharmacokinetic model of rifampicin for predicting drug-drug interactions via P-glycoprotein induction and inhibition in the intestine, liver, and kidney. *CPT Pharmacomet. Syst. Pharmacol.* **2022**, *11*, 919–933. [CrossRef] [PubMed]
104. Jamei, M.; Bajot, F.; Neuhoff, S.; Barter, Z.; Yang, J.; Rostami-Hodjegan, A.; Rowland-Yeo, K. A mechanistic framework for in vitro-in vivo extrapolation of liver membrane transporters: Prediction of drug-drug interaction between rosuvastatin and cyclosporine. *Clin. Pharmacokinet.* **2014**, *53*, 73–87. [CrossRef] [PubMed]
105. Sun, Y.; Chothe, P.P.; Sager, J.E.; Tsao, H.; Moore, A.; Laitinen, L.; Hariparsad, N. Quantitative Prediction of CYP3A4 Induction: Impact of Measured, Free, and Intracellular Perpetrator Concentrations from Human Hepatocyte Induction Studies on Drug-Drug Interaction Predictions. *Drug Metab. Dispos.* **2017**, *45*, 692–705. [CrossRef] [PubMed]
106. Li, N.; Badrinarayanan, A.; Ishida, K.; Li, X.; Roberts, J.; Wang, S.; Hayashi, M.; Gupta, A. Albumin-Mediated Uptake Improves Human Clearance Prediction for Hepatic Uptake Transporter Substrates Aiding a Mechanistic In Vitro-In Vivo Extrapolation (IVIVE) Strategy in Discovery Research. *AAPS J.* **2020**, *23*, 1. [CrossRef]
107. Riede, J.; Camenisch, G.; Huwyler, J.; Poller, B. Current In Vitro Methods to Determine Hepatic Kp(uu): A Comparison of Their Usefulness and Limitations. *J. Pharm. Sci.* **2017**, *106*, 2805–2814. [CrossRef] [PubMed]
108. Cremer, J.E.; Seville, M.P. Regional brain blood flow, blood volume, and haematocrit values in the adult rat. *J. Cereb. Blood Flow Metab.* **1983**, *3*, 254–256. [CrossRef] [PubMed]
109. Lee, H.B.; Blaufox, M.D. Blood volume in the rat. *J. Nucl. Med.* **1985**, *26*, 72–76. [PubMed]
110. Jobin, J.; Bonjour, J. Measurement of glomerular filtration rate in conscious unrestrained rats with inulin infused by implanted osmotic pumps. *Am. J. Physiol. Renal Physiol.* **1985**, *248*, F734–F738. [CrossRef] [PubMed]